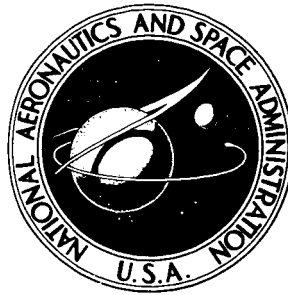


NASA TECHNICAL NOTE



NASA TN D-7403

NASA TN D-7403

**AERODYNAMIC HEATING AND LOADING
WITHIN LARGE OPEN CAVITIES
IN CONE AND CONE-CYLINDER-FLARE
MODELS AT MACH 6.7**

by L. Roane Hunt

*Langley Research Center
Hampton, Va. 23665*

AERODYNAMIC HEATING AND LOADING WITHIN LARGE OPEN CAVITIES IN CONE AND CONE-CYLINDER-FLARE MODELS AT MACH 6.7

By L. Roane Hunt
Langley Research Center

SUMMARY

The aerodynamic heating and loading distributions within large cavities exposed by surface openings to hypersonic flow were determined in the 8-foot high-temperature structures tunnel. Cone and cone-cylinder-flare models with cavities having regular and irregular surface-opening shapes were aerothermally tested at various angles of attack up to 30° . Tests were conducted at a Mach number of 6.7, a total temperature of 1800 K, a dynamic pressure of 80 kPa, and a stream unit Reynolds number of 6×10^6 per meter. The results showed that the heating rates at internal reattachment were generally lower but of the same order as the corresponding external heating rates; however, other internal heating rates were an order of magnitude lower. The internal flow showed characteristics of being funneled into jets or being dispersed dependent upon the internal surface contour.

INTRODUCTION

Successful atmospheric reentry of vehicles, such as intercontinental ballistic missiles or space shuttle vehicles, may be greatly jeopardized by surface openings which would expose interior cavities to hypersonic flow producing significant aerodynamic heating and loading and thereby causing the vehicle to be damaged. For ballistic missiles, the extent of damage produced by defensive weapons which would cause destruction of the missile upon reentry is of interest in determining weapon effectiveness, but this determination is most difficult. The space shuttle vehicle, which incorporates an external thermal protection system of ceramic tiles, could experience a similar problem with a surface opening if a tile or a portion of a surface panel was inadvertently lost. Other surface openings (or ports) are designed into reentry vehicles and proper account must be taken of the internal heating within the cavities.

The present aerothermal tests were made to determine the pressure and heating-rate distribution on the internal surfaces exposed by surface openings in typical reentry-shape models. Models with two cone configurations and a cone-cylinder-flare model with surface openings were tested in the 8-foot high-temperature structures tunnel at angles of attack up to 30° . These models were large in order to obtain realistic boundary-layer

conditions at the surface openings. To determine gas-addition effects on internal heating rates, one of the cones was tested with various ablation materials attached to a portion of the internal surfaces. Tests were made at a Mach number of 6.7, a total temperature of 1800 K, and a dynamic pressure of 80 kPa. The stream unit Reynolds number was 6×10^6 per meter.

SYMBOLS

The measurements and calculations were made in U.S. Customary Units but are given in the International System of Units (SI) as set forth in reference 1.

C_p	specific heat at constant pressure, J/kg-K
N_{Pr}	Prandtl number
N_{Re}	Reynolds number, based on wetted length from nose tip
N_{St}	Stanton number
p	pressure, Pa
q	heating rate, W/m ²
r	radial distance, m (see fig. 5(a))
s	wetted distance from top of bulkhead, m (see figs. 18, 19, and 20)
T	temperature, K
V	velocity, m/s
x	distance from model nose tip, m (see figs. 1 and 3)
α	angle of attack
β	angular location around models from center line on the forward bulkhead, deg (see fig. 5)
θ	angular location around models from center line of surface opening, deg (see figs. 1, 3, and 5)

ρ density, kg/m³

ϕ angular location from model center line on the rear bulkhead, deg (see figs. 5(b) and 5(c))

Superscript:

*

property evaluated at Eckert's reference temperature

Subscripts:

a average

aw adiabatic wall

e boundary-layer edge

w wall

Prefixes (see fig. 5):

C slug calorimeter

H Gardon heat-flux gage

P pressure orifice

T thermocouple

MODELS AND INSTRUMENTATION

Three model configurations were tested. Two of the models which were variations of the same basic 15° conical frustum are shown in figure 1. A 15° nose-cone section attached to the frustum formed a 15° cone designated model A; and a 19° nose-cone-cylinder section attached to the frustum formed a cone-cylinder-flare configuration, designated model B. The models had a nose radius of 0.3 cm and were stainless steel with a ring of 2-mm-diameter spheres (flow trip) welded 7.6 cm from the nose. A cutout in the surface provided an opening to an annular interior cavity. As shown by the dashed lines (fig. 1) the rear bulkhead of the cavity of the cone model was flat, whereas it was spherical for the rear bulkhead for the cone-cylinder-flare model. Photographs of models A and B mounted in test position are shown in figure 2.

Figure 3 shows a sketch of the third model, a blunt 9° cone. This model represents a reentry missile with a surface opening produced by an explosive charge to simulate X-radiation damage. This model, designated model C, was fabricated with an ablation surface of tape-wound silica phenolic. The surface opening was geometrically irregular; the internal annular cavity as shown by the dashed lines was similar to that for model B. A photograph of model C mounted in the test position is shown in figure 4.

The location of the model instrumentation is listed in table I. The instrumentation locations on the internal surfaces are indicated in figure 5 for the forward and rear bulkheads and the structural shell. The instrumentation consisted of pressure orifices (P), copper slug calorimeters (C), chromel-alumel thermocouples (T) attached to the backside of thin walls, and Gardon heat-flux gages (H).

FACILITY

The tests were conducted in the Langley 8-foot high-temperature structures tunnel which is shown schematically in figure 6. This facility is a hypersonic blowdown wind tunnel which operates at a nominal Mach number of 7, at total pressures between 3 and 24 MPa, and at nominal total temperatures between 1400 K and 2000 K. Corresponding free-stream unit Reynolds numbers are between 1×10^6 and 10×10^6 per meter. These conditions simulate the aerothermal flight environment at Mach 7 in the altitude range between 25 and 40 km.

The high-energy test medium is the combustion products of methane and air which are burned within a pressurized combustion chamber. Total temperature is controlled by regulating the fuel-to-air ratio. The combustion products are expanded to the test-section Mach number by means of an axisymmetric contoured nozzle which has an exit diameter of 2.4 m. In the test section, the stream is a free jet over a length of 4.3 m and then enters a straight tube diffuser where it is pumped to the atmosphere by means of a single-stage annular air ejector. The thermodynamic, transport, and flow properties of the combustion gases are computed by the methods set forth in reference 2.

Models are kept out of the stream until the test conditions are established. The model is then inserted rapidly (approximately 1 sec required) into the stream on an elevator. The model can be programed through a series of angles of attack as prescribed by test requirements. Prior to tunnel shutdown, the model is withdrawn from the stream.

Reference 3 presents a limited amount of test-stream survey results for the facility. Variations in pitot and static pressures and Mach number across a stream core diameter of 1 m for two longitudinal positions (1.45 m apart) are presented. The pitot and static pressures varied within ± 9 percent, both vertically and longitudinally. The free-stream Mach numbers determined from these pressures varied within ± 3 percent vertically and within ± 2 percent longitudinally.

DATA ACQUISITION AND REDUCTION

Data quantities were recorded on a high-speed digital data recording system at a rate of 20 samples per second. Typical data histories of model position, and model surface pressure, temperature, and heating rate are shown in figure 7. The test duration, as indicated in figure 7, is the time during which the model was within 15 cm of the tunnel center line. The "data-time" is the time within the test duration that the heating rates were a maximum and for which heating rates are specified in subsequent presentation of results. Heating rates were obtained from thermocouples, using thin-wall transient techniques, and Gardon heat-flux gages. Most of the pressures presented in subsequent tables are for the same "data-time" as the heating data; however, data for a later time are presented if the pressures in the orifice line had not reached a steady-state condition at the "data-time."

TESTS

All tests were made at the same tunnel condition. The combustor total pressure was 23.4 MPa with a ± 0.5 -percent variation and the combustor total temperature was 1800 K with a ± 4 -percent variation. These variations are equivalent to those that would occur during an individual test. The corresponding test stream Mach number, dynamic pressure, and static pressure for these tests were 6.7, 80 kPa, and 2.1 kPa, respectively. Test conditions for the three models are presented in table II. The model angle of attack, which is measured between the tunnel center line and the model center line, is positive with the surface opening on the windward side. The test durations are listed in table II.

Model A (fig. 1) was tested at an angle of attack of 0° with and without various ablation materials attached to the flat rear bulkhead of the cavity. Tests were made using polyurethane, polyethylene, and polyimide ablation materials as indicated in table II. The nominal thicknesses of the materials were 1.36, 1.27, and 0.635 cm, respectively. Model B (fig. 1) was tested at angles of attack from 0° to 30° and model C (fig. 3) was tested at angles of attack from 0° to 10° .

RESULTS AND DISCUSSION

Pressures and heat-transfer rates for selected "data-times" are listed in table III; and the temperature of the sensors, corresponding to the heating rates of table III, are listed in table IV. Heat-transfer data from sensors with known damage (such as the extensive erosion of the teflon insulator around the external slug calorimeter that occurred during run 1) or questionable response have been omitted. Pressure data that had not fully stabilized during the test (sensor P29 and P34 of tests 9 and 10) are also omitted. As shown in table IV, the temperatures of some of the sensors in the areas of highest

heating approached 800 K at the selected times; however, no attempt has been made to adjust the data to obtain cold-wall heating rates or to correct for the effects of radiation or conduction.

External Aerothermodynamics

Flow characteristics.— The character of the external flow over the cone models (models A and C) is indicated by the schlieren photographs presented in figure 8. These photographs correspond to tests of models A and C at angles of attack of 0° and 10° , respectively. The center line of the surface opening was positioned on the upper ridgeline of the models and the schlieren system was positioned to give a view of the flow at the surface opening. There are many weak shock waves in each of the photographs caused by surface irregularities. For model A shock waves can be traced to where the model parts are joined, the fairings around the surface openings, and the surface sensors. The wavy irregular surface of model C (see fig. 4) caused numerous shock waves to emanate from its surface. In figure 8 the dark region extending from the front edge to the rear edge of the surface opening is the spreading shear layer. The flow impingement on the rear of the opening produces a strong shock wave which can be seen. In fact, this wave (fig. 8(b)) intersects the bow shock wave.

Figure 9 presents schlieren photographs of the flow over the cone-cylinder-flare configuration, model B, for various angles of attack. The schlieren-system position relative to model B was the same as that for the models previously described and similar weak shock waves from surface irregularities were evident in figure 9. At $\alpha = 0^\circ$ (fig. 9(a)) the flow is turned 15° producing a compression shock wave. It also appears that flow separation occurs at this point which was expected. For this case the shear layer is not as clearly defined as for the conical models. The tendency of the flow to separate is reduced with angle of attack because the flow is dispersed around the body away from the higher pressure region. However, the flow pattern is complicated by the bow-shock-wave interference for the higher angles of attack. In figure 9(c) the shear layer appears to be affected by the bow wave which intersects the model near the center of the surface opening.

Pressure and heating-rate distributions.— Measured exterior pressures and heating rates for model A ($\alpha = 0^\circ$) and model B ($\alpha = 0^\circ, 10^\circ, 21^\circ$, and 30°) are presented as functions of axial distance in figures 10 and 11, respectively, and compared with calculated distributions obtained from two different theoretical approaches. The first theoretical approach was the Lockheed hypersonic inlet program, reference 4, which incorporates the method of characteristics for the inviscid flow with appropriate boundary-layer solutions. The heating rates for laminar and turbulent boundary layers were obtained from the Cohen and the Lockheed integral methods, respectively. The beginning of transition was assumed

to occur at the flow trip. For the second analytical approach, the surface pressure was obtained by using tangent cone theory and the surface heating rate by using the Blasius turbulent-boundary-layer solution presented in reference 5. Boundary-layer gas properties were evaluated at Eckert's reference temperature. The wetted surface distance from the nose tip was included in determining the local Reynolds number. Therefore, the heating rate determined from the latter method is expressed as follows:

$$q = \rho_e^* V_e C_p^* \left[0.0348 (N_{Pr}^*)^{-2/3} (N_{Re}^*)^{-1/5} \right] (T_{aw} - T_w) \quad (1)$$

In figure 10, the results from model A are well predicted by theory. The measured surface pressures are within ± 1 percent of the predicted value of 14.5 kPa. The surface heating rates at $x = 26$ cm as determined by the three data points at different circumferential locations ranged from 0.545 to 0.579 MW/m², which indicated that an evenly distributed turbulent boundary layer was obtained ahead of the surface opening. The heating rates immediately behind the surface opening were 0.431 and 0.465 MW/m². The results at both longitudinal locations were within ± 7 percent of the prediction of equation (1).

The theory of reference 4 was limited in predicting the pressure and heating-rate distributions for model B (fig. 11) in that (1) a flow solution along the surface of the flare could not be obtained using the method of characteristics because of convergence problems and (2) no solution was obtained at $\alpha = 30^\circ$ because the total angle of nose cone surface was 49° with the free-stream flow producing near subsonic local velocities. The pressure distributions on model B were excellently predicted by theory for $\alpha = 0^\circ$ and 10° , and a maximum deviation of ± 16 percent occurred on the flare for the higher angles of attack. The two heating-rate data points at $x = 24$ cm for $\alpha = 0^\circ$ (fig. 11(a)) were obtained on opposite sides of the 19° cone. The 0.550 and 0.567 MW/m² heating-rate values are just below the turbulent heating rate predicted by each theory. It is concluded that the transition produced by the boundary-layer flow trip was evenly distributed. The heating-rate distribution was well predicted by theory, but at $\alpha = 30^\circ$ the maximum deviation was 32 percent on the flare.

Heating correlation.— The heating results obtained from the conical nose sections of models A and B are presented in figure 12. The nondimensional heat-transfer coefficient, Stanton number, is plotted as a function of the Reynolds number. These parameters are based on local flow conditions, Eckert's reference temperature, and the wetted length from the nose tip. Laminar and turbulent theory (ref. 5), indicated in figure 12, are expressed as

$$N_{St}^* = 0.575 (N_{Pr}^*)^{-2/3} (N_{Re}^*)^{-1/2} \quad (\text{Laminar})$$

$$N_{St}^* = 0.0348 (N_{Pr}^*)^{-2/3} (N_{Re}^*)^{-1/5} \quad (\text{Turbulent})$$

Data from reference 6 for a 36° cone tested in the Langley 8-foot high-temperature structures tunnel with natural transition are also presented.

The present results from the test of model A (circular symbols) fall on the turbulent theory curve. (The data for the two Reynolds numbers correspond to the two longitudinal locations of the model slug calorimeters.) The results from the 19° nose cone of model B are indicated by the square symbols with the flags on the symbol indicating different model angles of attack. (The results of this model at $\alpha = 30^\circ$ are much higher than the prediction (fig. 11(d)); and since the effective cone angle was large and the local flow condition uncertain, these data are not included in fig. 12.) The data of model B fall within the scatter of the reference 6 data with the possible exception of the $\alpha = 0^\circ$ data, which are relatively low. These results indicate a good correlation of the heating to cones in the present facility.

Internal Aerothermodynamics

Flow characteristics.— The internal space exposed by the surface openings of each model is indicated in figures 1, 2, and 5 and the various exposed surfaces are labeled in figure 5. Also, figure 5 shows the instrumentation location for each surface that is used for determining internal surface heating rates. As indicated in the model description, models A and B have the same internal surfaces except for the shape of the rear bulkhead which has an appreciable effect on the volume of the space and the flow path within this space.

The internal flow within model A with the flat rear bulkhead differed from the other models, because the shear layer (fig. 8) impinged on the rear lip of the opening. Consequently, the gas experienced shock losses, then separated from the lip, and reattached on the surface of the rear bulkhead. In the test series of model A, various ablation materials were placed in front of the flat rear bulkhead to determine the effect of the ablating gas within the internal cavity. Ablation of material did not significantly reduce the heating to exposed surfaces within the cavity.

The charring of the materials made visible the flow-impingement pattern. A photograph taken of the polyurethane material (viewed through the surface opening) is shown in figure 13. The char pattern indicates an unsymmetrical impingement to the right of center. Also shown in figure 13 is a sketch of the recession contours which indicate a maximum recession of 6 mm off center by about 1.5 cm. The projection of the surface openings is

indicated in the sketch. There was no measured misalignment of the model. Moreover, the char pattern on the polyimide material resulting from test 4 indicated the darkest char immediately behind the surface opening and lighter char away from that region with apparent symmetry. No char pattern was obtained for the polyethylene material, because all of the material was ablated during the test.

The internal flow within model B was complicated by the complex external flow discussed earlier – external flow separation at $\alpha = 0^\circ$ and shock interference at higher values of α . The impingement of the shear layer occurred on the spherical rear bulkhead with no secondary reattachment as in the case of model A.

The internal flow pattern for model C is demonstrated in the photographs presented as figure 14. The photographs were taken from a position directly above the surface opening with the model apex to the left. The edges of the opening expose the various construction layers: rough exterior of ablation material; aluminum sheet; foam insulation; and the instrumented rear bulkhead. The pretest condition of the model is shown in figure 14(a). The individual sensors are clearly visible in all the photographs and aid in correlating the extent of model deterioration. A photograph of the model after test 11 in figure 14(b) shows the groove in the foam at the pencil point which indicates that the flow was funneled into a jet. The flow path appeared to be relatively narrow and straight down the center of the opening. In figure 14(c), which is a photograph of the model after test 12 ($\alpha = 10^\circ$), the foam is burned away and the impingement area is broadened. Solidified droplets of aluminum and resin indicate that the flow was dispersed over the spherical bulkhead.

Pressure.– The limited internal pressure results are presented in table III. (Very little pressure variation within the cavities was anticipated; therefore, only a minimal amount of pressure instrumentation was located internally.) At the lower angles of attack the measured pressure levels within the cavity are about equal to the experimental and theoretical external pressures at the surface openings shown in figures 10 and 11. However, for model B at $\alpha = 30^\circ$ the internal pressure at the bottom of the rear bulkhead (P57) was 23 percent above the theoretical pressure of the model surface indicated in figure 11(d) and the internal pressure near the reattachment area (P51) was 62 percent above the external pressure. The increased internal pressure was probably a result of the interaction of the bow and compression shocks above the opening.

Angular heating-rate distribution.– The internal heating-rate distributions for the models tested are presented in figures 15, 16, and 17 as functions of θ . The distributions are plotted for the rear and forward bulkheads for all models and for the structural shell for the models that were instrumented. The angular width of the surface opening is represented by the vertical dashed lines for the models A and B. The results from sensors located 180° from the center line of the opening are plotted twice, at $\theta = 180^\circ$ and -180° .

The results from model A at $\alpha = 0^\circ$ are presented in figure 15. The instrumentation coverage appeared to be adequate to indicate the internal heating-rate distributions on the various components. Results obtained on the rear bulkhead are plotted for various radius locations r . The curves are faired symmetrically about the center line of the surface opening with only one data point on the right side at $\theta = -90^\circ$ to substantiate this assumption. Actually, the flow pattern indicated by the photograph of figure 13 of a similar test was not symmetric and the high heating would be slightly to the right of center. The expected impingement would be a broad radial line behind the opening, but the data and the photograph of figure 13 suggest a funneling of the flow to a core which has a concentrated impingement point. The maximum measured heating rate was about 0.140 MW/m^2 occurring on the surface opening center line at $r = 11.2 \text{ cm}$, which was the same radial location as indicated by the recession contour sketch of figure 13. This heating rate was about 30 percent of the external surface heating at the surface opening as indicated in figure 15. The heating to the structural shell seemed to be symmetrical and the highest heating occurred at $\theta = 180^\circ$. The heating to the forward bulkhead was not symmetrical and the highest heating occurred on the right side.

Similar results for model B with a spherical rear bulkhead are presented in figure 16 for various angles of attack. The most significant heating occurred on the rear bulkhead immediately behind the surface opening. The heating-rate distribution behind the opening for all angles of attack was symmetrical and was nearly flat as a function of the angle ϕ . The maximum heating rates to the rear bulkhead for the various angles of attack were generally lower but of same order as the external heating rate at the opening. The heating rates to the other internal surfaces were an order of magnitude lower, except at higher angles of attack where the heating to the structural shell was significant. The results of model C, which also had a spherical rear bulkhead, show a similar pattern in figure 17 where the most significant heating occurred behind the surface opening.

Heating-rate variation along internal surfaces in flow direction.— The internal area experiencing the most significant heating was the rear bulkhead area behind the surface opening as was indicated by figures 15, 16, and 17. The heating results for this area are presented in figures 18, 19, and 20 as a function of the distance s along the surface of the rear bulkhead in the flow direction. The distance s is defined in the sketch at the top of each figure. As indicated in figure 15, the maximum heating to model A occurred at $r = 11.2 \text{ cm}$ or, in figure 18, at $s = 4.61 \text{ cm}$. A dashed, faired curve indicates the heating distribution with four data points at $\theta = 0^\circ$. Only two data points were available for the other values of θ . Heating rates for model B are presented in figure 19 as a function of s for each angle of attack tested. The heating-rate values presented are an average of those presented in figure 16 across the width of the surface opening. These results indicate a smooth decrease in heating rate with distance s and an increase in heating rate with angle of attack.

In figure 20 the internal heating rate for model C is plotted against the distance s which is along the surface opening center line across the rear bulkhead, center section, and the forward bulkhead. The faired curves indicate a decrease in heating rate with distance s and an increase in heating rate with angle of attack. The apparent reduction in heating rate at $s = 18$ cm is probably caused by flow separation at the juncture of the rear bulkhead and the center section.

Heating-rate variations with angle of attack.— In general, the magnitude of the external heating rate to model B near the opening increased directly with angle of attack. Also the internal heating, which is related to the local external flow, varied with angle of attack. The heating rates measured on the various internal areas of model B were averaged and plotted as a function of α in figure 21. These areas included the lower half of the rear bulkhead, the structural shell, and the forward bulkhead. In all cases the upper half of the rear bulkhead experienced the greater heating load. At $\alpha = 0^\circ$ and 10° the order of decreasing heating was the forward bulkhead, structural shell, and lower rear bulkhead, but at $\alpha = 30^\circ$ the order was changed to the structural shell, lower rear bulkhead, and the forward bulkhead. This shift in the heating distribution was a result of a shift in the flow path from primarily within the pitch plane to a circumferential path.

CONCLUSIONS

An investigation was made in the Langley 8-foot high-temperature structures tunnel to study the internal flow effects in large internal cavities exposed by large surface openings in typical reentry-shape models. Cone and cone-cylinder-flare models with regular and irregular shaped surface openings were tested at angles of attack up to 30° . Tests were made at a Mach number of 6.7, a total temperature of 1800 K, and a dynamic pressure of 80 kPa. The stream unit Reynolds number was 6×10^6 per meter. The following conclusions are indicated:

1. External pressure and heating-rate distributions on the models agreed with theoretical predictions.
2. Internal pressures were about equal to the external surface pressure to which the cavity was exposed.
3. Internal heating rates to areas of direct flow impingement were generally lower but of the same order as the heating rate to the surface to which the cavity was exposed, with both the external and internal heating rates increasing with angle of attack. Internal heating rates decreased with distance from the impingement area by as much as an order of magnitude.
4. The internal flow showed characteristics of being funneled into jets or being dispersed dependent upon the internal surface contours. Also, the internal-flow direction is affected by model angle of attack.

5. Ablation of material attached to the rear bulkhead did not significantly reduce the heating rate to exposed surfaces within the cavity.

Langley Research Center,
National Aeronautics and Space Administration,
Hampton, Va., October 31, 1973.

REFERENCES

1. Anon.: Metric Practice Guide. E 380-72, Amer. Soc. Testing Mater., June 1972.
2. Leyhe, E. W.; and Howell, R. R.: Calculation Procedure for Thermodynamic, Transport, and Flow Properties of the Combustion Products of a Hydrocarbon Fuel Mixture Burned in Air With Results for Ethylene-Air and Methane-Air Mixtures. NASA TN D-914, 1962.
3. Deveikis, William D.; and Hunt, L. Roane: Loading and Heating of a Large Flat Plate at Mach 7 in the Langley 8-Foot High-Temperature Structures Tunnel. NASA TN D-7275, 1973.
4. Maslowe, S. A.; and Benson, J. L.: Computer Program for the Design and Analysis of Hypersonic Inlets. Rep. No. 18079 (Contract NAS 2-1460), Lockheed-California Co., Aug. 10, 1964. (Available as NASA CR-77749.)
5. Kays, W. M.: Convective Heat and Mass Transfer. McGraw-Hill Book Co., Inc., c.1966.
6. Hunt, L. Roane; and Bruce, W. E., Jr.: Experimental Study of Groove Patterns on Ablated Surfaces in the Langley 8-Foot High-Temperature Structures Tunnel. NASA TM X-2030, 1970.

TABLE I.- LOCATION OF INSTRUMENTATION FOR MODELS TESTED IN
8-FOOT HIGH-TEMPERATURE STRUCTURES TUNNEL

(a) Model A

Sensor	x, cm	θ , deg	r, cm	β , deg	Sensor	x, cm	θ , deg	r, cm
Pressure orifices					Slug calorimeters			
^a P13	44.7	0			^a C19	24.1	0	
^a P14	42.7	0			^a C20	24.1	28.7	
^a P16	42.7	90			^a C22	24.1	180	
^a P21	24.1	90			^a C43	66.8	0	
^a P23	12.1	0			^a C45	66.8	28.7	
^a P44	66.8	14.35			C49		28.7	11.2
P57		135	11.2		C50		90	11.2
Thermocouples					C52		0	15.0
T19		0	5.09		C53		180	7.56
T20		14.35	11.2		C55		0	7.56
T21		14.35	15.0		C56		90	15.0
T22		42.6	15.0		C58		0	11.2
T23		90	5.09		C76		270	11.2
T24		180	11.2		C77		28.7	15.0
T25		315		39	C80		180	15.0
T26		225		39	C200	56.8	90	
T27		135		39	C201	56.8	180	
T28		45		39	C202	56.8	270	
					C203	49.3	90	
					C204	49.3	180	
					C205	49.3	270	

^aExternal instrumentation.

TABLE I.- LOCATION OF INSTRUMENTATION FOR MODELS TESTED IN
8-FOOT HIGH-TEMPERATURE STRUCTURES TUNNEL - Continued

(b) Model B

Sensor	x, cm	θ , deg	ϕ , deg	β , deg	Sensor	x, cm	θ , deg	ϕ , deg
Pressure orifices					Slug calorimeters			
^a P26	66.0	0			^a C33	54.4	28.7	
^a P27	64.0	0			^a C36	36.7	0	
^a P29	64.0	90			^a C37	24.0	0	
^a P32	54.4	0			^a C40	24.0	180	
^a P34	54.4	90			^a C43	88.1	28.7	
^a P39	24.0	90			^a C45	88.1	0	
^a P41	11.9	0			C49		0	15
^a P44	88.1	14.35			C50		0	30
P51		0	41		C52		331.3	41
P57		180	41		C53		316.4	30
Thermocouples					C55		270	41
T8		345.65	30		C56		331.3	15
T9		345.65	43		C58		28.7	41
T10		316.4	14		C76		331.3	30
T11		316.4	43		C77		225	30
T12		270	14		C80		14.35	30
T13		180	30		C200	78.1	90	
T14		90	30		C201	78.1	180	
T15		90	43		C202	78.1	270	
T16		28.7	14		C203	70.5	90	
T17		28.7	30		C204	70.5	180	
T18		14.35	43		C205	70.5	270	
T25		315		39				
T26		225		39				
T27		135		39				
T28		45		39				

^aExternal instrumentation.

TABLE I.- LOCATION OF INSTRUMENTATION FOR MODELS TESTED IN
8-FOOT HIGH-TEMPERATURE STRUCTURES TUNNEL – Concluded

(c) Model C

Sensor	x, cm	θ , deg	ϕ , deg	β , deg
Pressure orifices				
^a P1	60.6	270	39.5	42
P2		270		
P3		0		
^a P4	100.1	270		
Gardon heat-flux gages				
H1		180	73	42
H2		0		
H3		330		
H4		300		
H5		0		
H6		322		
H7		292		
H8		270		
H9		0		
H10		0		
Slug calorimeters				
C1		0	33	42
C2		90		42
C3		322		
C4		292		
C5		322		
C6		292		
C7		180		
C8		180		
^b C9	78.7		46	

^aExternal instrumentation.

^b_r = 5.09 cm.

TABLE II. - TEST CONDITIONS FOR MODELS

Test	α , deg	Test duration, sec	Internal albatation material
Model A			
1	0	8.9	None
2	0	16.0	Polyurethane
3	0	14.6	Polyethylene
4	0	18.1	Polyimide
Model B			
5	0	5.9	
6	10.0	4.6	
7	21.1	1.8	
8	21.2	1.6	
9	30.0	.3	
10	30.0	.8	
Model C			
11	0	21.2	
12	10.0	33.9	

TABLE III.- PRESSURE AND HEAT-TRANSFER RATE^a FOR
THE SELECTED DATA TIME

(a) Model A; $\alpha = 0^\circ$

Sensor	Test 1	Test 2	Test 3	Test 4	Sensor	Test 1	Test 2	Test 3	Test 4
Pressure, kPa					Heating rate, kW/m ²				
P13	14.2	15.7	15.7	15.9	C19	579	(b)	(b)	(b)
P14	15.7	15.7	15.7	15.9	C20	556	(b)	(b)	(b)
P16	15.6	15.3	15.4	15.0	C22	545	(b)	(b)	(b)
P21	15.7	15.5	15.7	15.6	C43	431	(b)	(b)	(b)
P23	14.0	13.6	13.2	13.7	C45	465	(b)	(b)	(b)
P44	15.0	15.3	15.2	15.9	C49	97.6	0	0	0
P57	15.9	16.0	16.4	16.4	C50	53.3	0	0	0
Heating rate, kW/m ²					C52	73.8	0	(c)	(c)
T19	109.0	0	0	0	^d C53				
T20	122.6	0	0	0	C55	111.2	0	0	0
T21	67.0	0	0	0	^d C56				
T22	50.0	0	0	0	C58	139.6	0	0	0
T23	84.0	0	0	0	C76	48.8	0	0	0
T24	46.5	0	0	0	C77	54.5	0	0	0
T25	35.1	35.1	37.4	42.0	C80	40.8	0	0	0
T26	39.7	37.4	51.1	39.7	C200	30.7	37.4	27.3	52.2
T27	25.0	34.0	25.0	22.7	C201	38.6	36.3	52.2	48.8
T28	19.3	19.3	22.7	19.3	C202	29.5	45.4	35.1	34.0
					C203	23.8	30.6	30.6	26.1
					C204	31.8	(c)	(c)	(c)
					C205	21.6	31.8	26.1	22.7

^aConversion: kPa \times 0.1450 = psia; kW/m² \times 0.0881 = Btu/ft²-sec.

^bSensor damaged during run 4.

^cErratic response.

^dSensor inoperative.

TABLE III.- PRESSURE AND HEAT-TRANSFER RATE^a FOR
THE SELECTED DATA TIME – Continued

(b) Model B

Sensor	Test 5 $\alpha = 0^\circ$	Test 6 $\alpha = 10.0^\circ$	Test 7 $\alpha = 21.1^\circ$	Test 8 $\alpha = 21.2^\circ$	Test 9 $\alpha = 30.0^\circ$	Test 10 $\alpha = 30.0^\circ$	Sensor	Test 5 $\alpha = 0^\circ$	Test 6 $\alpha = 10.0^\circ$	Test 7 $\alpha = 21.1^\circ$	Test 8 $\alpha = 21.2^\circ$	Test 9 $\alpha = 30.0^\circ$	Test 10 $\alpha = 30.0^\circ$
Pressure, kPa							Heating rate, kW/m ²						
P26	7.2	24.8	46.1	46.1	78.5	80.0	C33	39.7	168	368	357	482	545
P27	5.0	16.1	35.6	35.5	62.0	63.4	C36	54.5	181.6	485	454	649	704
P29	4.6	4.5	6.0	5.5	(c)	(e)	C37	567	1067	1362	1515	1748	1816
P32	2.6	5.7	17.4	17.2	31.7	32.4	C40	550	210	81.2	79.4	87.4	121.4
P34	2.1	2.1	3.2	3.2	(e)	(e)	C43	420	987	1475	1589	2100	2326
P39	20.5	19.7	18.4	17.4	15.8	18.6	C45	301	709	1169	1254	1214	1475
P41	17.7	40.4	81.2	80.9	106.7	108.1	C49	61.3	136.2	295	296	351	436
P44	13.7	33.1	71.6	68.5	80.6	93.0	C50	111.2	254	500	495	704	726
P51	14.8	32.8	74.4	75.1	143.2	144.6	C52	238.3	651	771	894	1668	1793
P57	12.1	27.6	60.3	59.9	105.4	108.1	C53	109.0	219	498	465	692	692
Heating rate, kW/m ²							C55	18.2	38.6	148.7	129.4	340	379
T8	126.0	233.8	447	409	567	616	C56	36.3	97.6	254	224	274	278
T9	366.6	582	(f)	(f)	1248	(c)	C58	281.5	480	851	794	1134	1271
T10	25.0	81.7	234	216	335	323	C76	51.1	126	435	396	562	582
^d T11	----	----	----	----	----	----	C77	12.5	25.0	72.6	71.5	126	138.5
T12	10.2	22.7	68.1	68.1	102.1	147.6	C80	132.8	263	536	503	726	783
T13	6.8	14.8	(c)	(c)	(c)	(c)	C200	25.0	59.0	239	227	470	454
T14	30.6	(c)	(c)	(c)	(c)	(c)	C201	9.1	18.2	79.4	79.4	213	176
T15	15.9	37.4	113.4	107.8	238	250	C202	19.3	43.1	176	165	319	362
T16	49.9	113.4	259	247	344	355	C203	44.3	74.9	230	219	303	236
T17	109.0	204	414	386	(c)	(c)	C204	14.8	27.2	62.4	57.9	94.2	115.8
T18	350.7	(c)	(c)	(c)	(c)	(c)	C205	28.4	47.7	177	172	151	184
T25	22.7	57.9	110.1	115.8	119.2	124.8							
T26	11.3	22.7	56.7	56.7	81.7	119.2							
T27	36.3	71.5	113.4	105.5	162.3	151.0							
T28	61.3	86.3	115.8	113.4	156.6	140.0							

^aConversion: kPa \times 0.1450 = psia; kW/m² \times 0.0881 = Btu/ft²-sec.

^cErratic response.

^dSensor inoperative.

^eSteady state not attained.

^fData over scale.

TABLE III.- PRESSURE AND HEAT-TRANSFER RATE^a FOR
THE SELECTED DATA TIME - Concluded

(c) Model C

Sensor	Test 11 $\alpha = 0^0$	Test 12 $\alpha = 10.0^0$
Pressure, kPa		
P1	5.4	5.2
P2	5.2	17.0
P3	5.2	16.6
P4	5.8	6.6
Heating rates, kW/m ²		
H1	9.1	29.5
H2	293	785
dH3	----	
dH4	----	
H5	94.2	244
H6	14.8	30.6
H7	9.1	39.7
H8	5.7	26.1
H9	46.5	210
H10	11.4	126
C1	11.4	103.3
C2	23.3	70.4
C3	14.8	(c)
C4	10.2	21.6
C5	7.9	38.6
C6	5.7	30.6
C7	7.9	31.8
C8	10.2	42.0
C9	29.5	135.1

^aConversion: kPa \times 0.1450 = psia; kW/m² = Btu/ft²-sec.

^cErratic response.

^dSensor inoperative.

TABLE IV.- TEMPERATURES (K) AT THE SELECTED DATA TIME
FOR EACH THERMOCOUPLE LOCATION

(a) Model A; $\alpha = 0^\circ$

Sensor	Temperature, K, for –				Sensor	Temperature, K, for –			
	Test 1	Test 2	Test 3	Test 4		Test 1	Test 2	Test 3	Test 4
C19	328	(a)	(a)	(a)	T19	367	297	298	294
C20	327	(a)	(a)	(a)	T20	375	297	296	294
C22	324	(a)	(a)	(a)	T21	340	298	298	298
C43	324	(a)	(a)	(a)	T22	329	297	298	296
C45	322	(a)	(a)	(a)	T23	349	297	297	294
C49	326	297	298	295	T24	324	296	296	291
C50	312	297	298	294	T25	326	329	328	332
C52	308	298	(b)	(b)	T26	330	329	332	321
^c C53					T27	320	329	321	321
C55	328	297	298	294	T28	317	318	318	319
^c C56									
C58	315	297	298	294					
C76	310	297	298	294					
C77	313	297	298	295					
C80	309	297	298	298					
C200	308	308	307	304					
C201	308	306	308	306					
C202	306	309	307	304					
C203	305	306	306	302					
C204	306	302	298	296					
C205	304	306	305	302					

^aSensor damaged during run 1.

^bErratic response.

^cSensor inoperative.

TABLE IV.- TEMPERATURES (K) AT THE SELECTED DATA TIME
FOR EACH THERMOCOUPLE LOCATION – Continued

(b) Model B

Sensor	Temperature, K, for –						Sensor	Temperature, K, for –					
	Test 5 $\alpha = 0^\circ$	Test 6 $\alpha = 10.0^\circ$	Test 7 $\alpha = 21.1^\circ$	Test 8 $\alpha = 21.2^\circ$	Test 9 $\alpha = 30.0^\circ$	Test 10 $\alpha = 30.0^\circ$		Test 5 $\alpha = 0^\circ$	Test 6 $\alpha = 10.0^\circ$	Test 7 $\alpha = 21.1^\circ$	Test 8 $\alpha = 21.2^\circ$	Test 9 $\alpha = 30.0^\circ$	Test 10 $\alpha = 30.0^\circ$
C33	313	322	370	342	365	359	T8	376	407	554	469	525	503
C36	312	329	388	349	389	378	T9	480	533	(b)	(b)	774	(b)
C37	323	333	356	326	340	337	T10	316	337	441	387	406	399
C40	321	301	303	300	298	297	^c T11						
C43	319	333	376	338	363	363	T12	304	306	348	329	347	348
C45	311	321	354	382	333	335	T13	294	289	(b)	(b)	(b)	(b)
C49	312	318	366	336	356	341	T14	317	(b)	(b)	(b)	(b)	(b)
C50	324	334	419	370	396	394	T15	307	309	354	342	382	379
C52	357	420	550	423	612	599	T16	331	348	448	392	426	406
C53	324	337	407	371	392	389	T17	363	387	523	447	(b)	(b)
C55	302	301	341	325	352	352	T18	483	(b)	(b)	(b)	(b)	(b)
C56	306	313	352	333	333	331	T25	311	322	373	342	353	348
C58	326	333	388	357	379	375	T26	305	308	354	331	345	349
C76	310	319	394	362	379	372	T27	326	334	380	348	383	360
C77	299	298	320	311	318	315	T28	338	332	376	345	369	357
C80	331	346	424	380	417	403							
C200	305	307	369	344	373	363							
C201	327	298	323	313	327	320							
C202	302	303	349	329	349	348							
C203	308	308	349	330	342	329							
C204	300	298	315	307	311	309							
C205	303	302	341	324	322	322							

^bErratic response.

^cSensor inoperative.

TABLE IV.- TEMPERATURES (K) AT THE SELECTED DATA TIME
FOR EACH THERMOCOUPLE LOCATION – Concluded

(c) Model C

Sensor	Temperature, K, for –	
	Test 11 $\alpha = 0^{\circ}$	Test 12 $\alpha = 10.0^{\circ}$
C1	301	307
C2	301	306
C3	301	(b)
C4	301	304
C5	301	304
C6	301	304
C7	301	304
C8	301	304
C9	302	308

^bErratic response.



(a) Model A.

L-71-6754

Figure 2.- Photograph of models A and B in the
8-foot high-temperature structures tunnel.



(b) Model B.

L-71-7342

Figure 2.- Concluded.

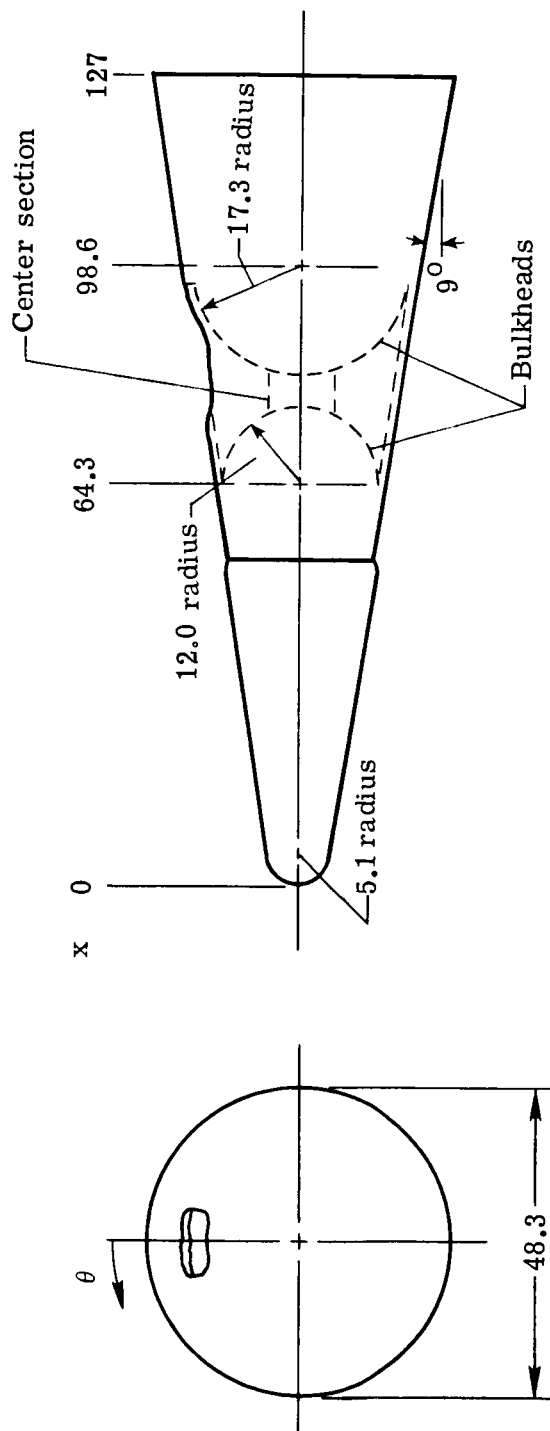
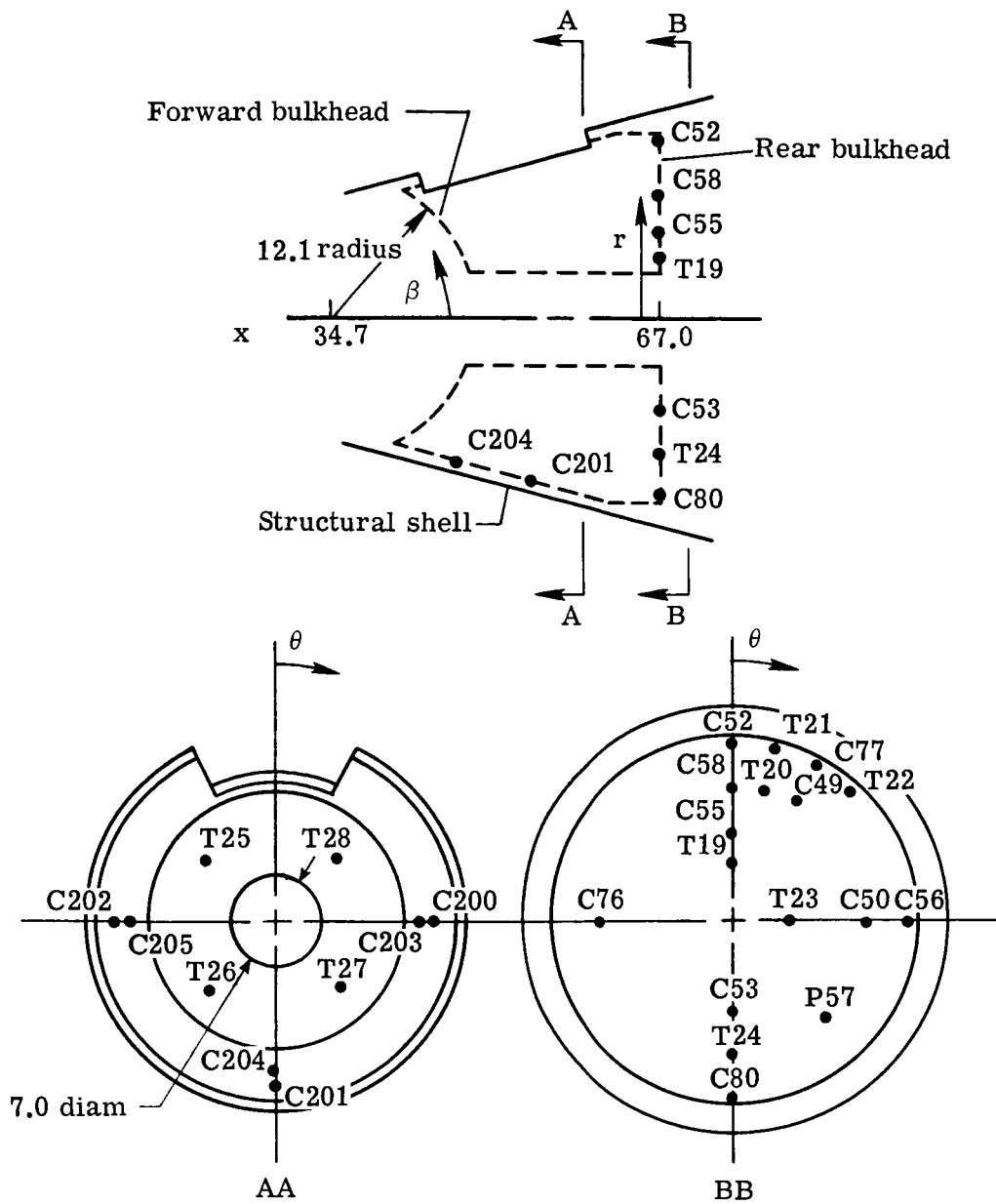


Figure 3.- Sketch of model C. All dimensions in cm.



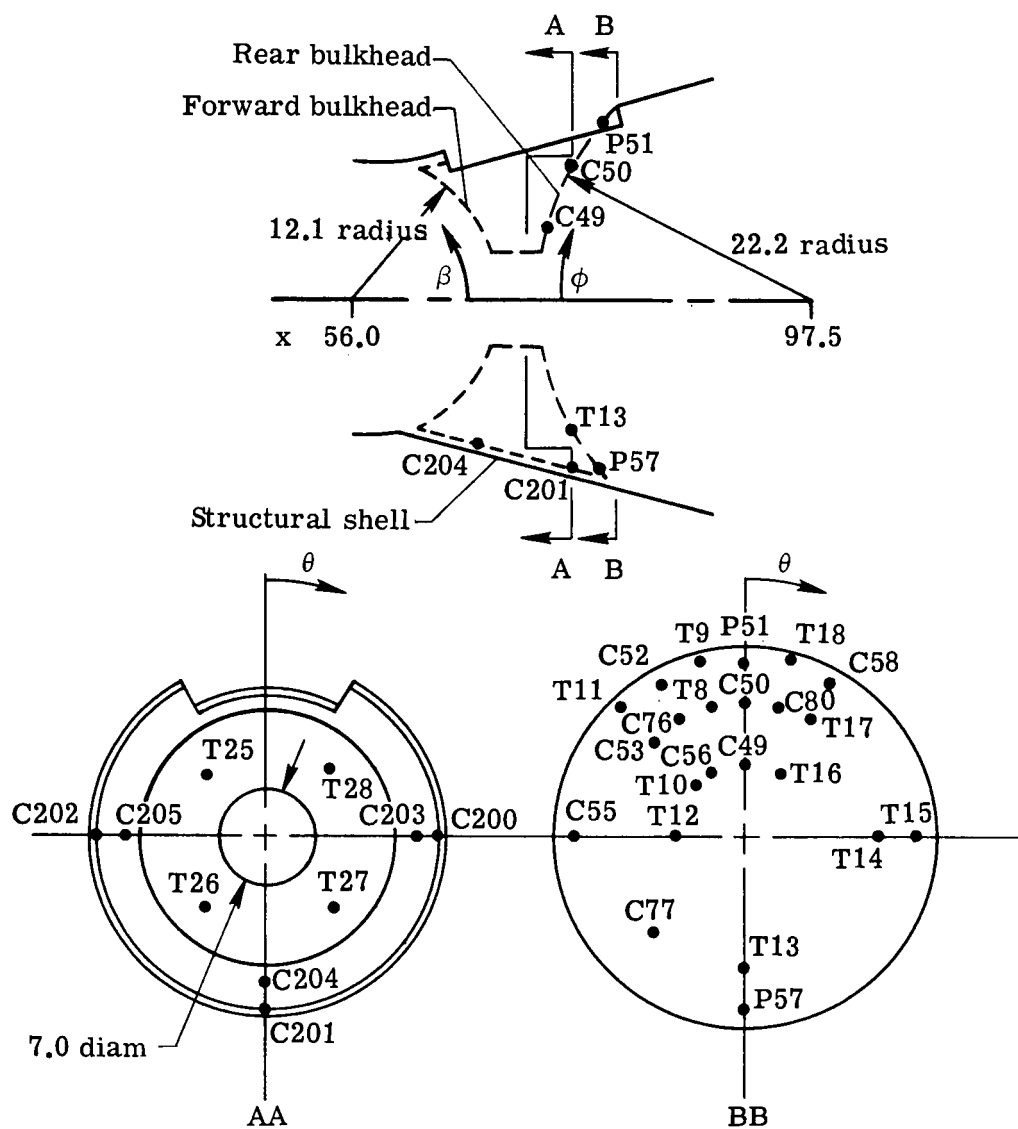
L-71-6825

Figure 4.- Photograph of model C in the 8-foot high-temperature structures tunnel.



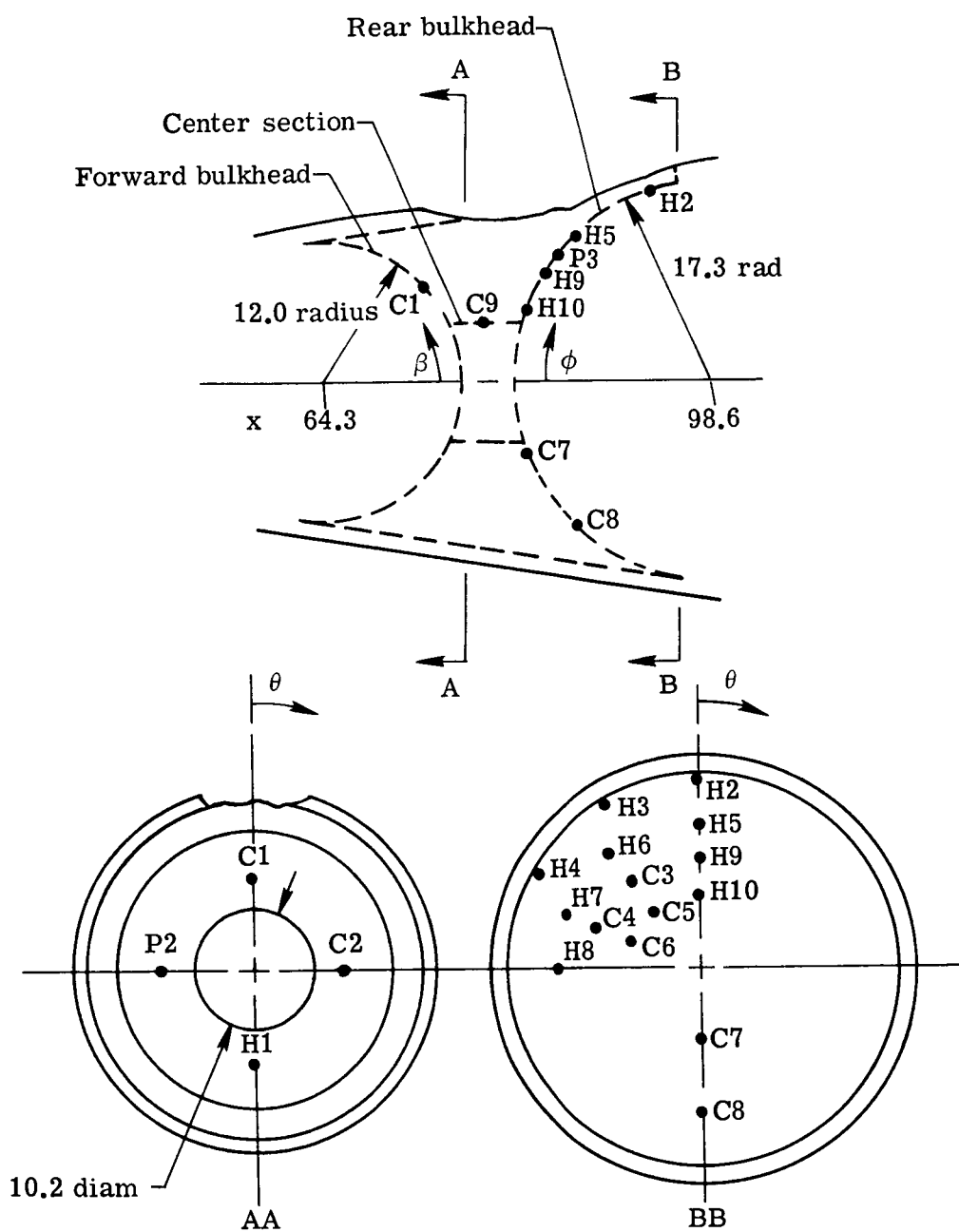
(a) Model A.

Figure 5.- Sketch of models indicating location of internal instrumentation.
All dimensions in cm.



(b) Model B.

Figure 5.- Continued.



(c) Model C.

Figure 5.- Concluded.

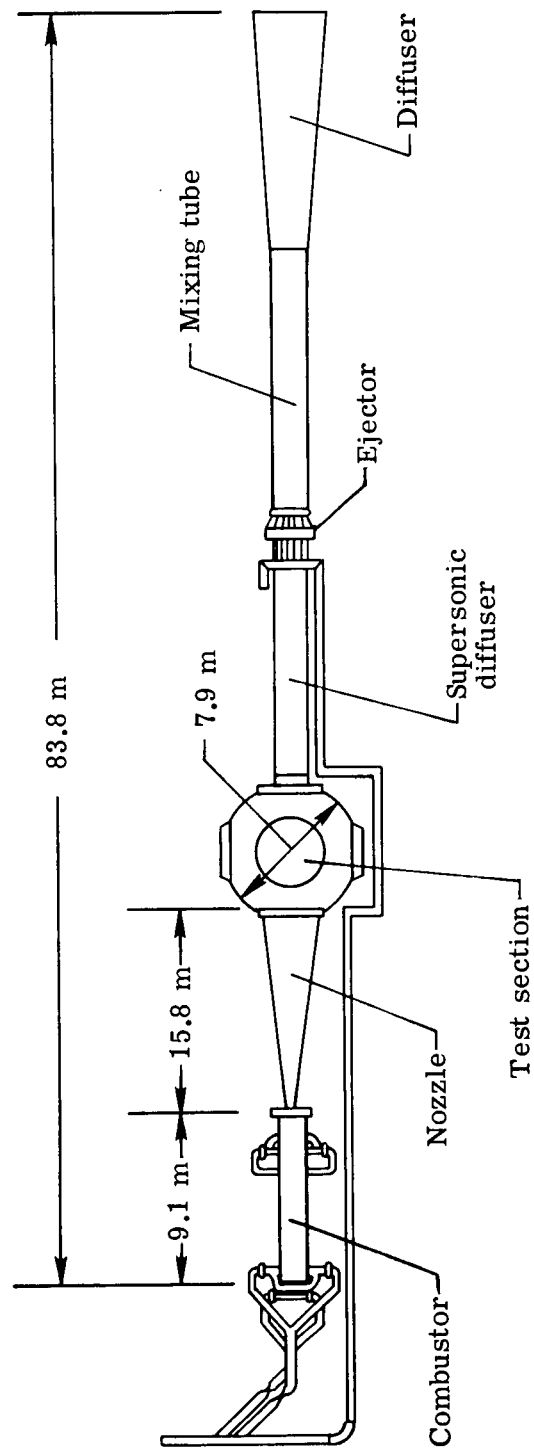


Figure 6. - Schematic drawing of the Langley 8-foot high-temperature structures tunnel.

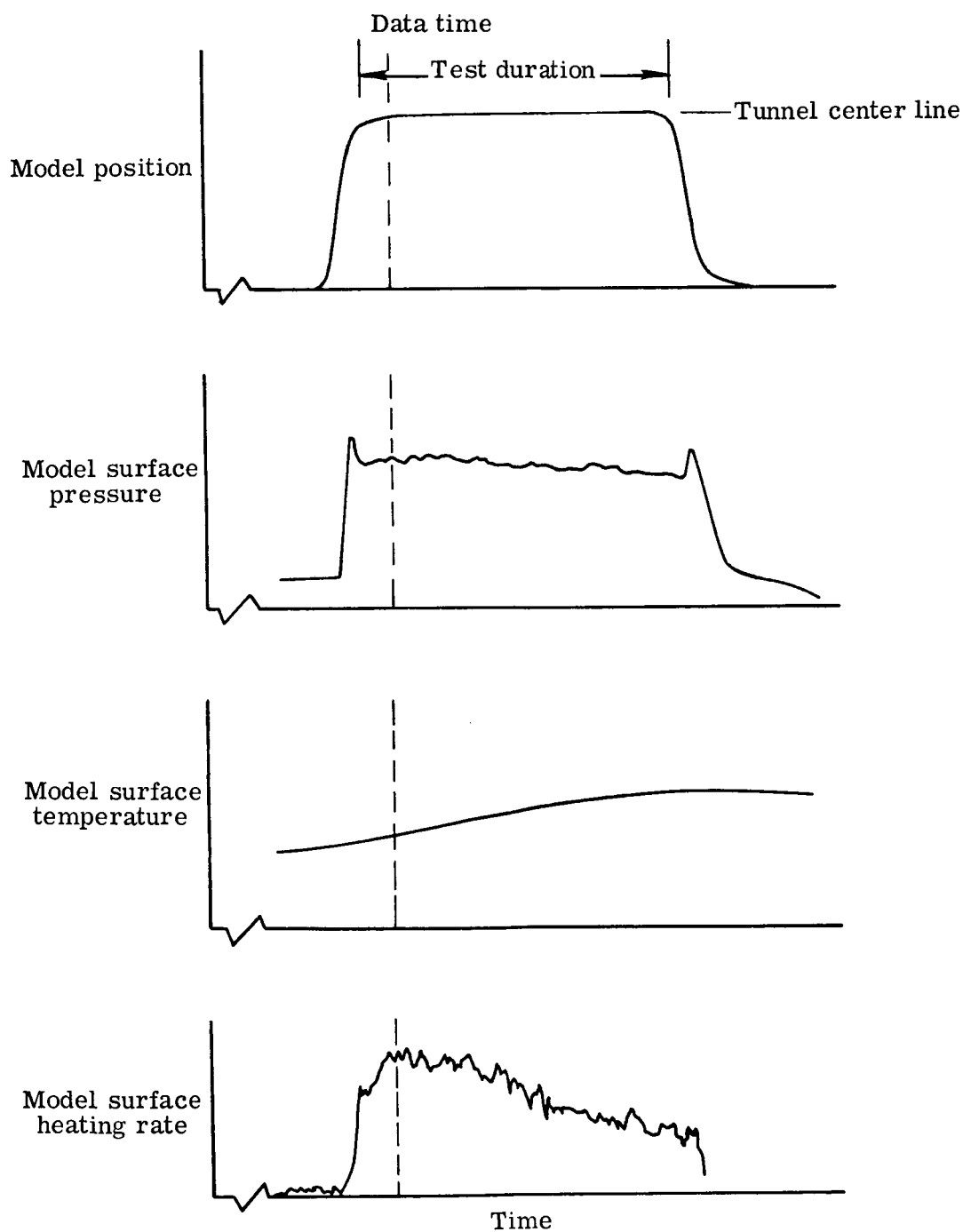
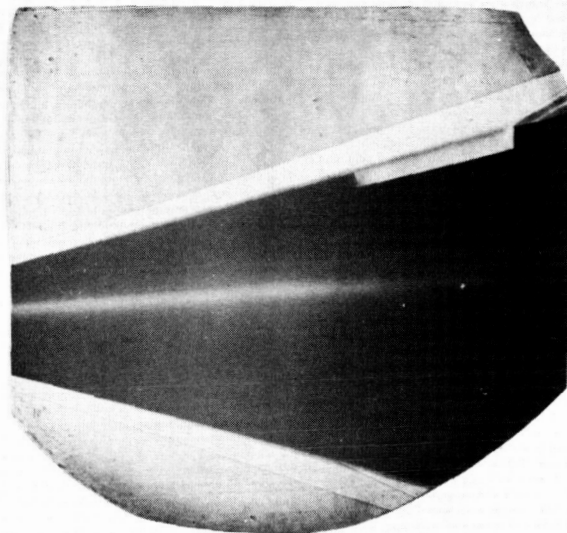


Figure 7.- Typical data acquisition and reduction.



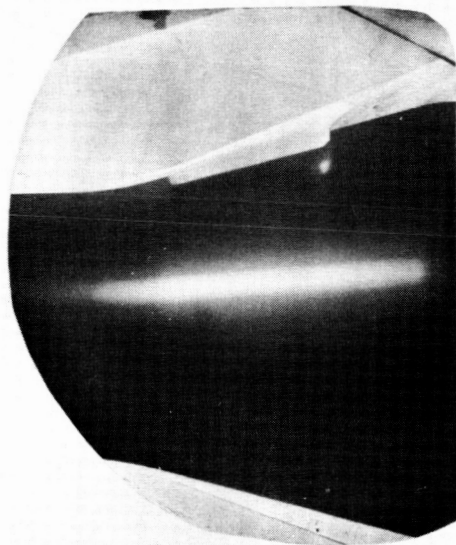
(a) Model A ($\alpha = 0^\circ$).



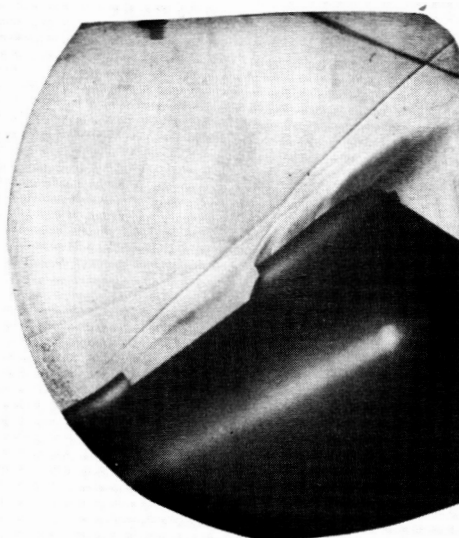
(b) Model C ($\alpha = 10^\circ$).

L-73-8018

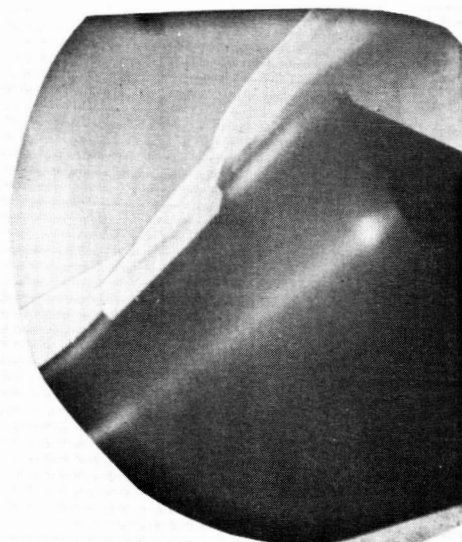
Figure 8.- Schlieren photographs of the area above the surface openings of the conical models.



(a) $\alpha = 0^\circ$.



(b) $\alpha = 21^\circ$.



(c) $\alpha = 30.0^\circ$.

Figure 9.- Schlieren photographs of the area
above the surface opening of model B.

L-73-8019

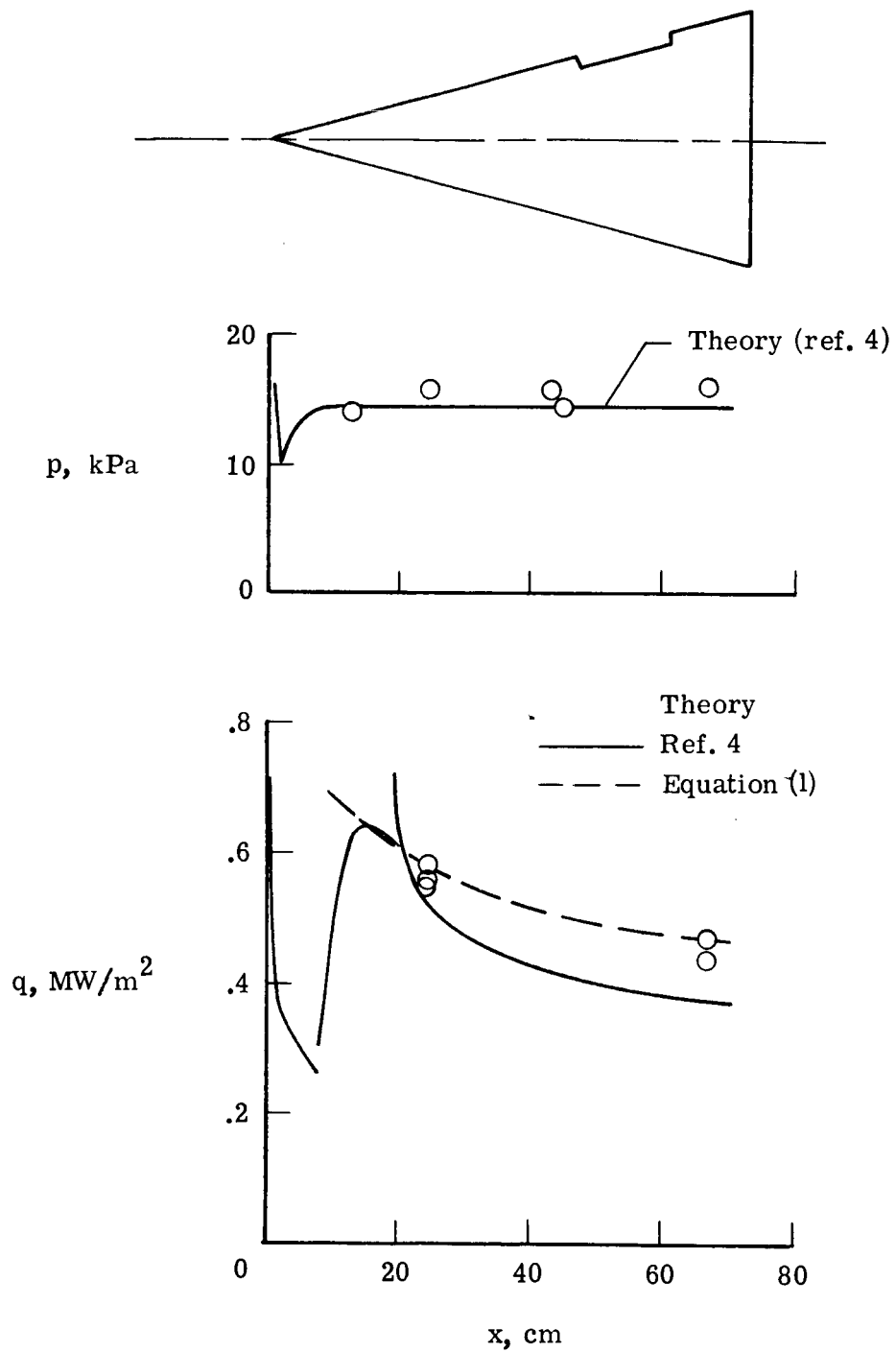
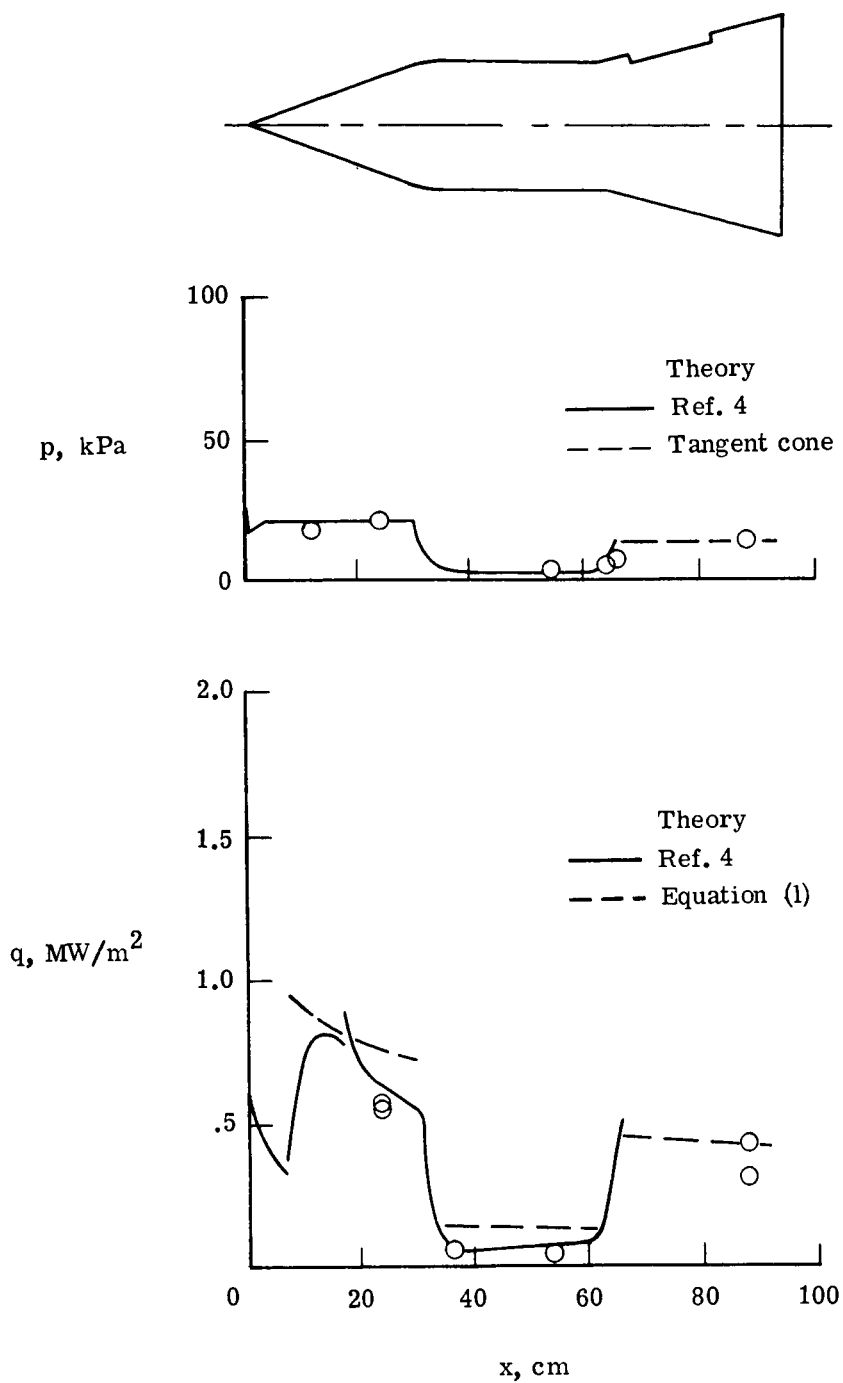
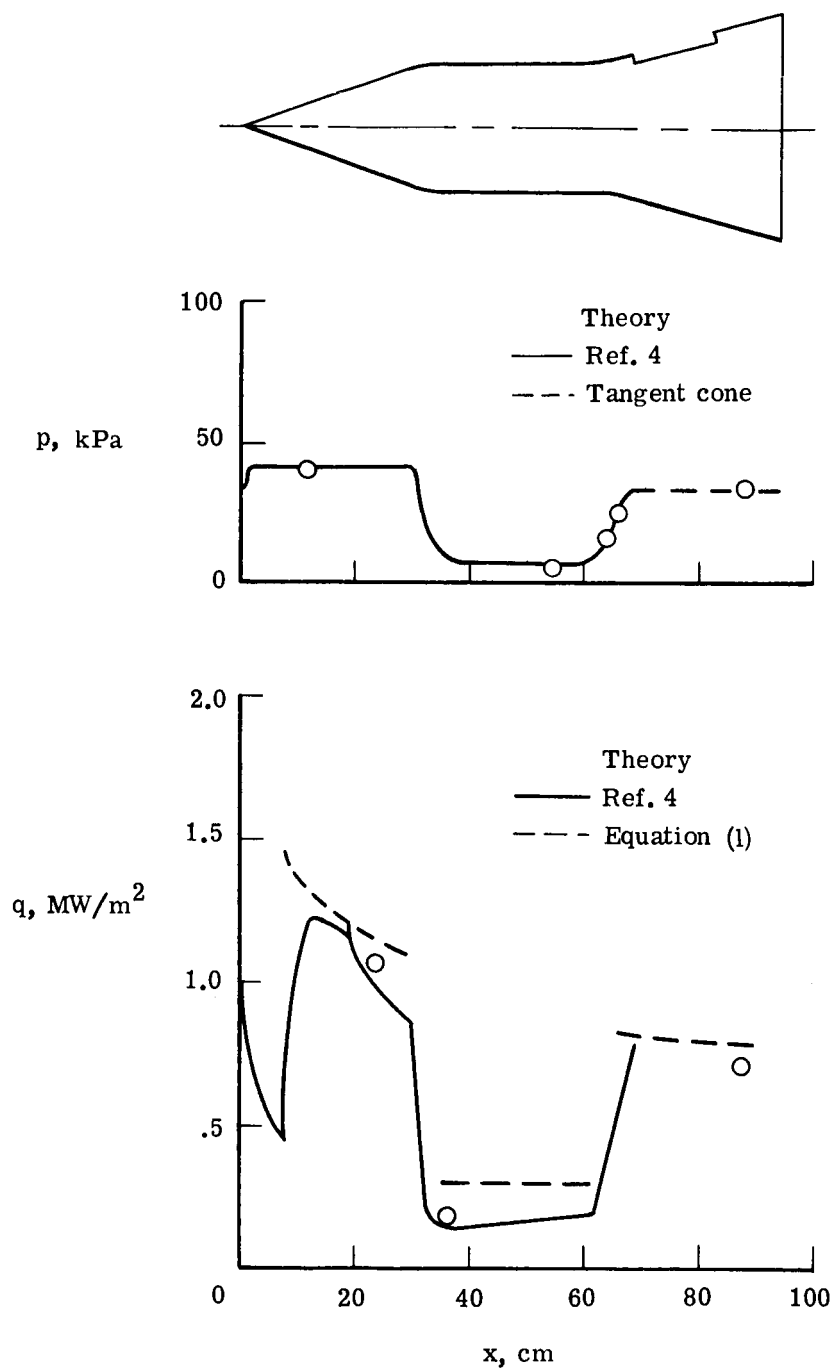


Figure 10.- Pressure and heating-rate distribution along surface of model A.



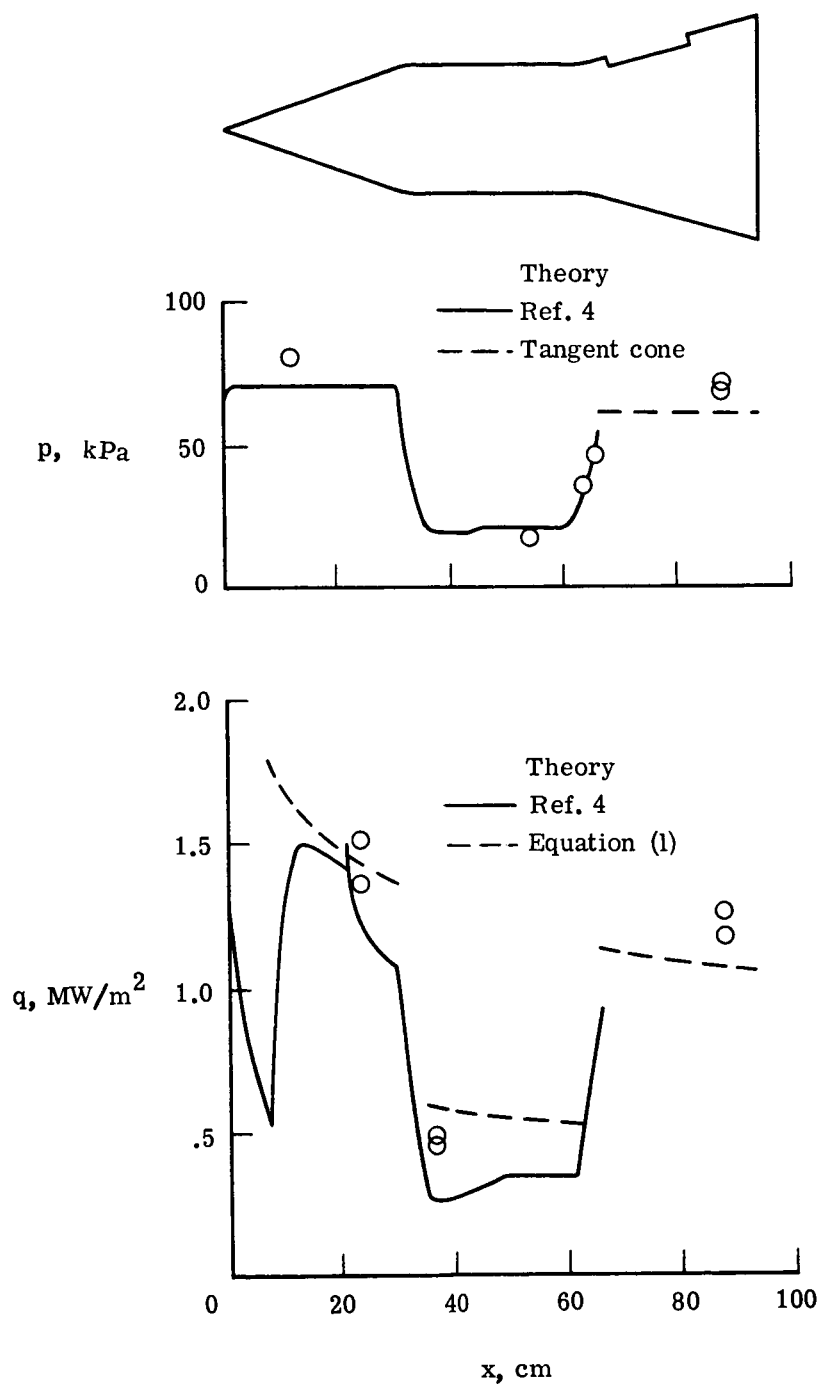
(a) $\alpha = 0^\circ$.

Figure 11.- Pressure and heating rate distribution along surface of model B at various angles of attack.



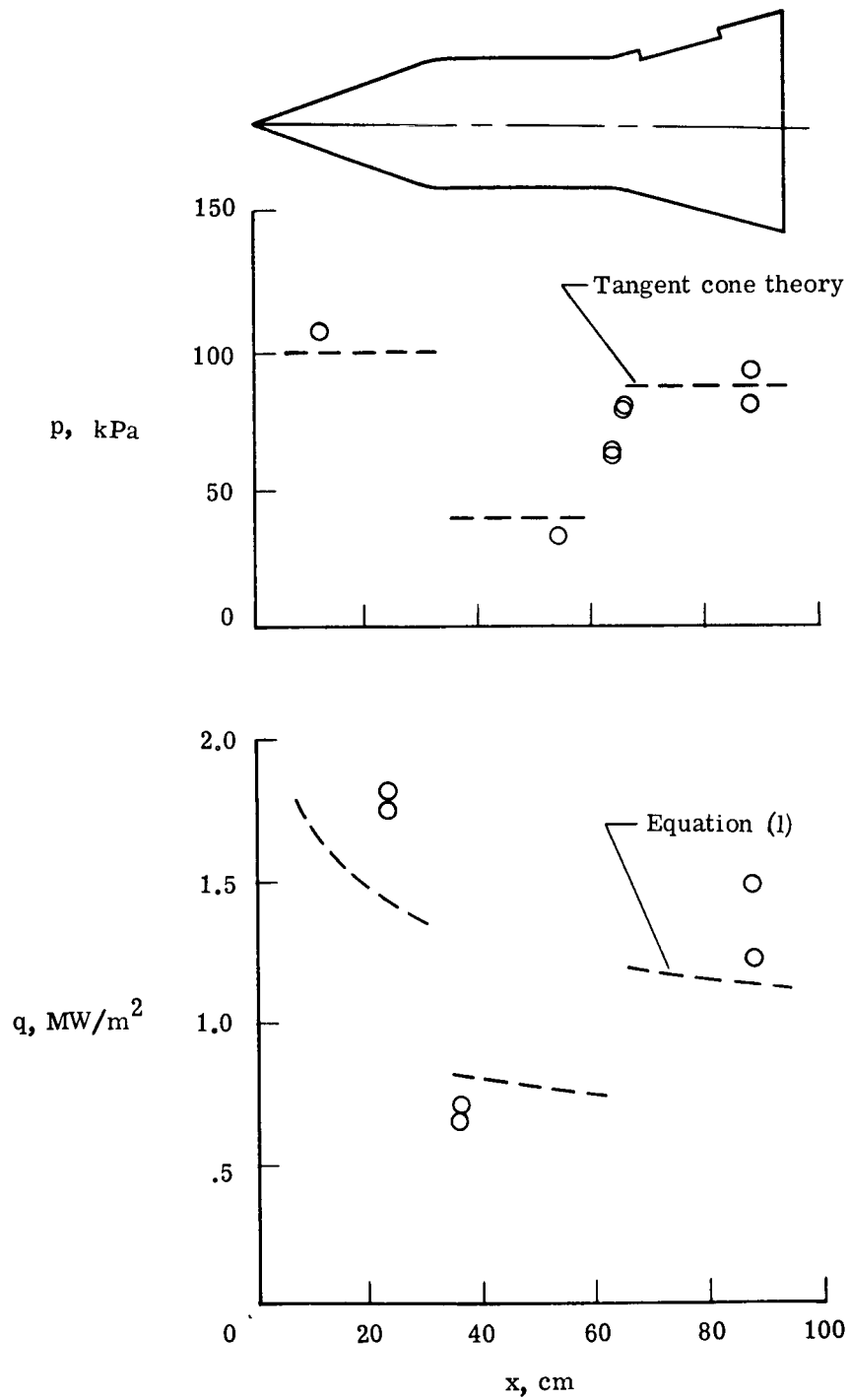
(b) $\alpha = 10^\circ$.

Figure 11.- Continued.



(c) $\alpha = 21^\circ$.

Figure 11.- Continued.



(d) $\alpha = 30^\circ$.

Figure 11.- Concluded.

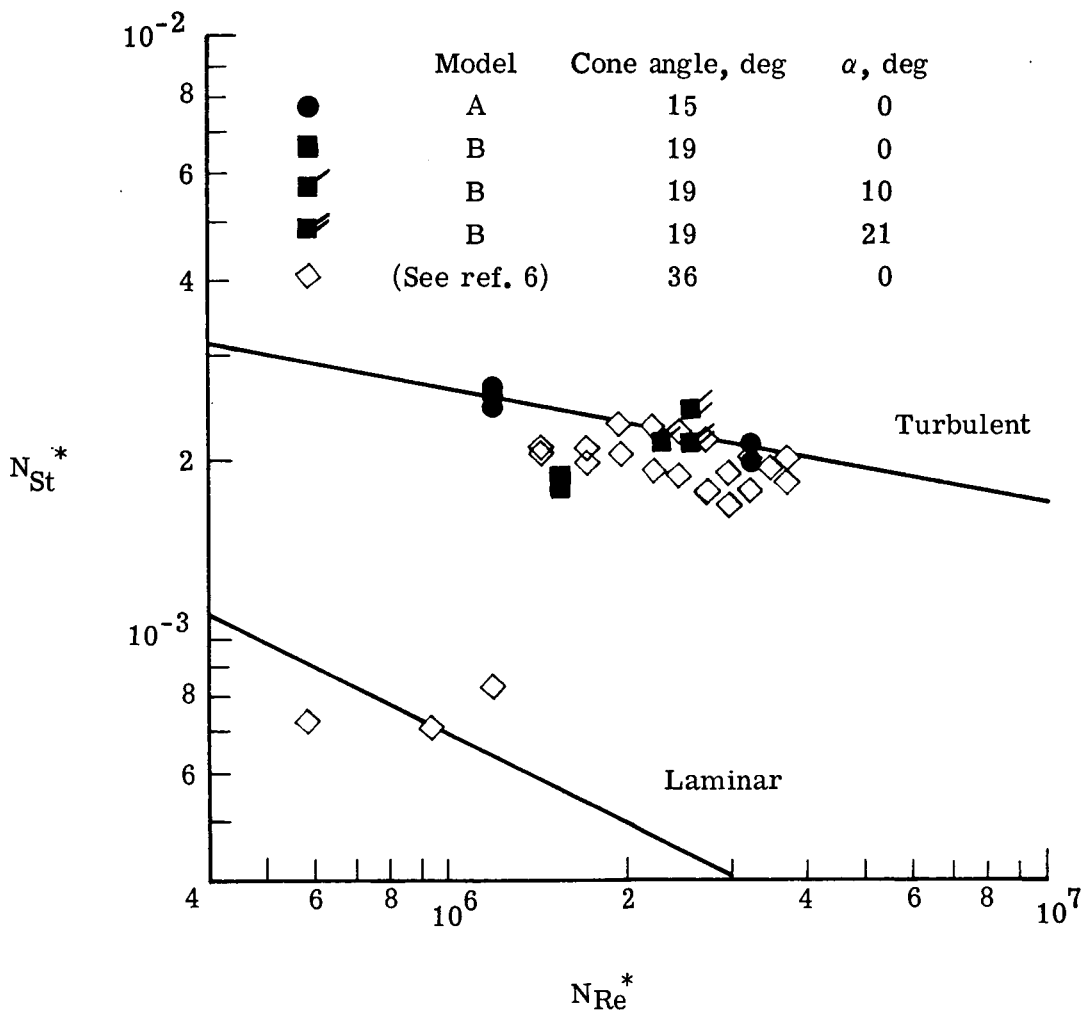
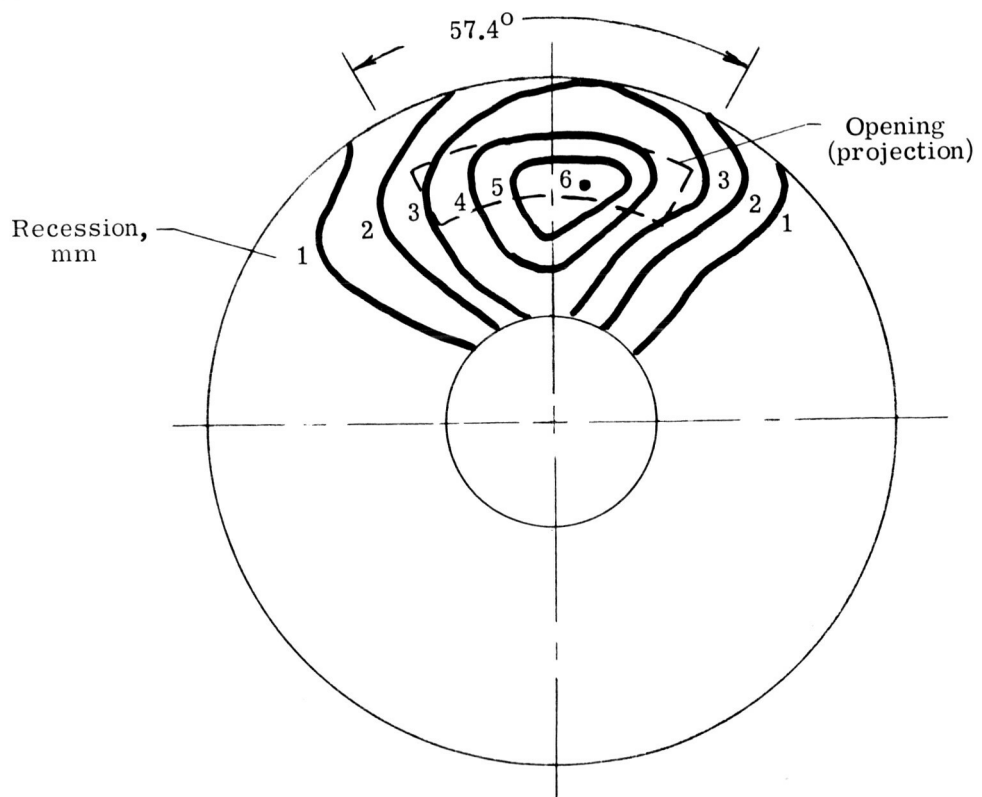
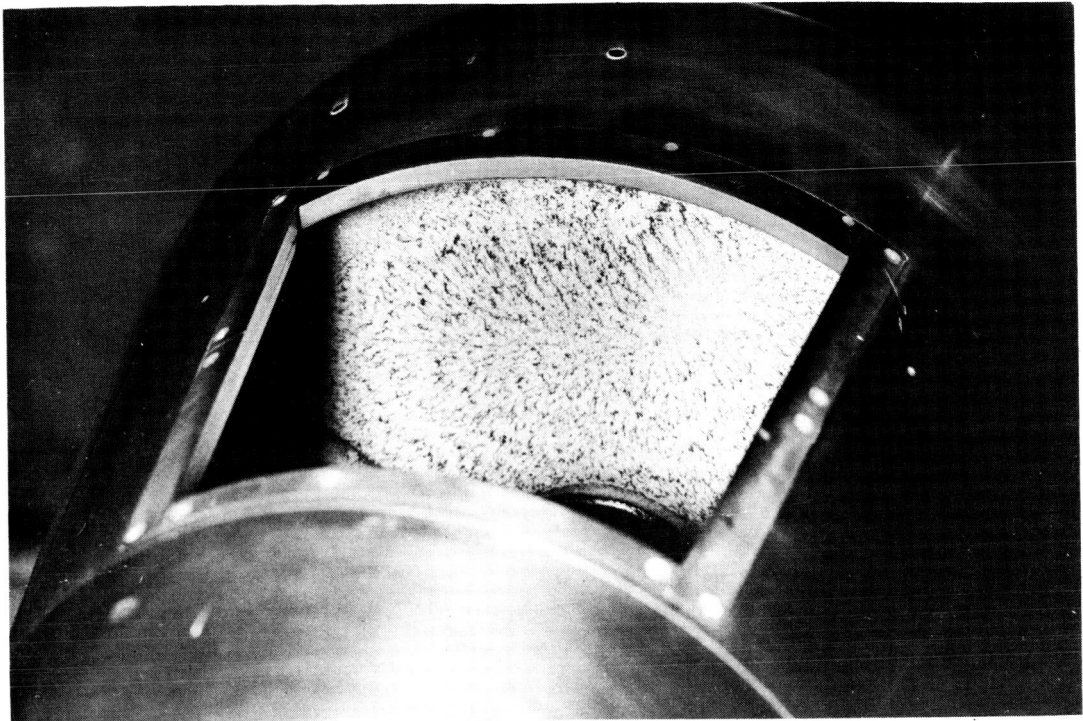
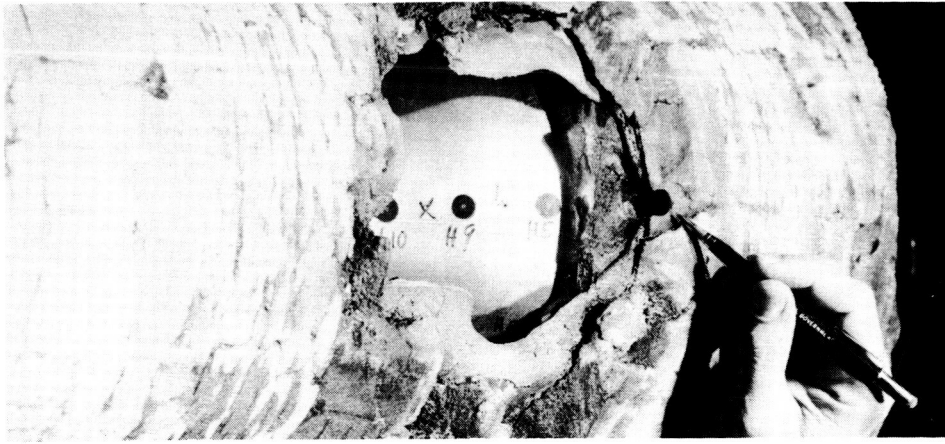


Figure 12.- Correlation of aerodynamic heating on cones in the 8-foot high-temperature structures tunnel.

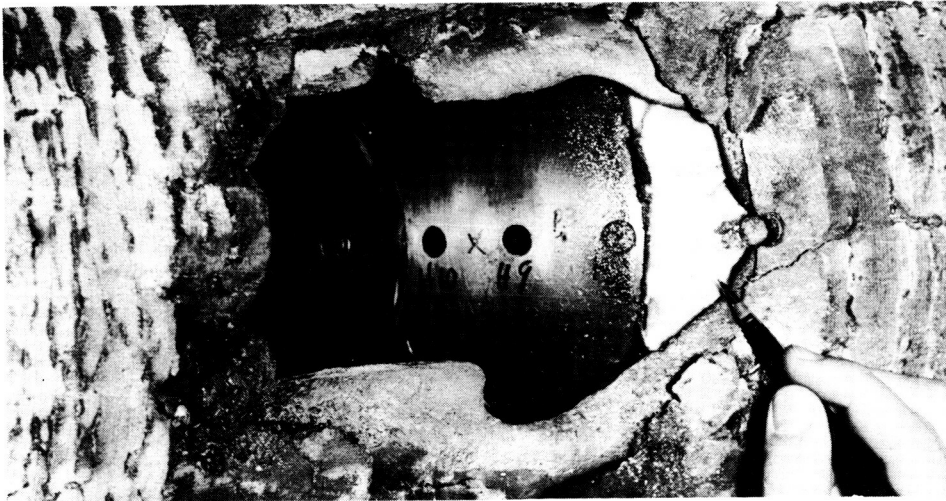


L-73-8020

Figure 13.- Photograph and sketch of polyurethane insert after test.



(a) Before test 11.



(b) After test 11.



(c) After test 12.

L-73-8021

Figure 14.- Photographs of the surface opening of model C before and after testing.

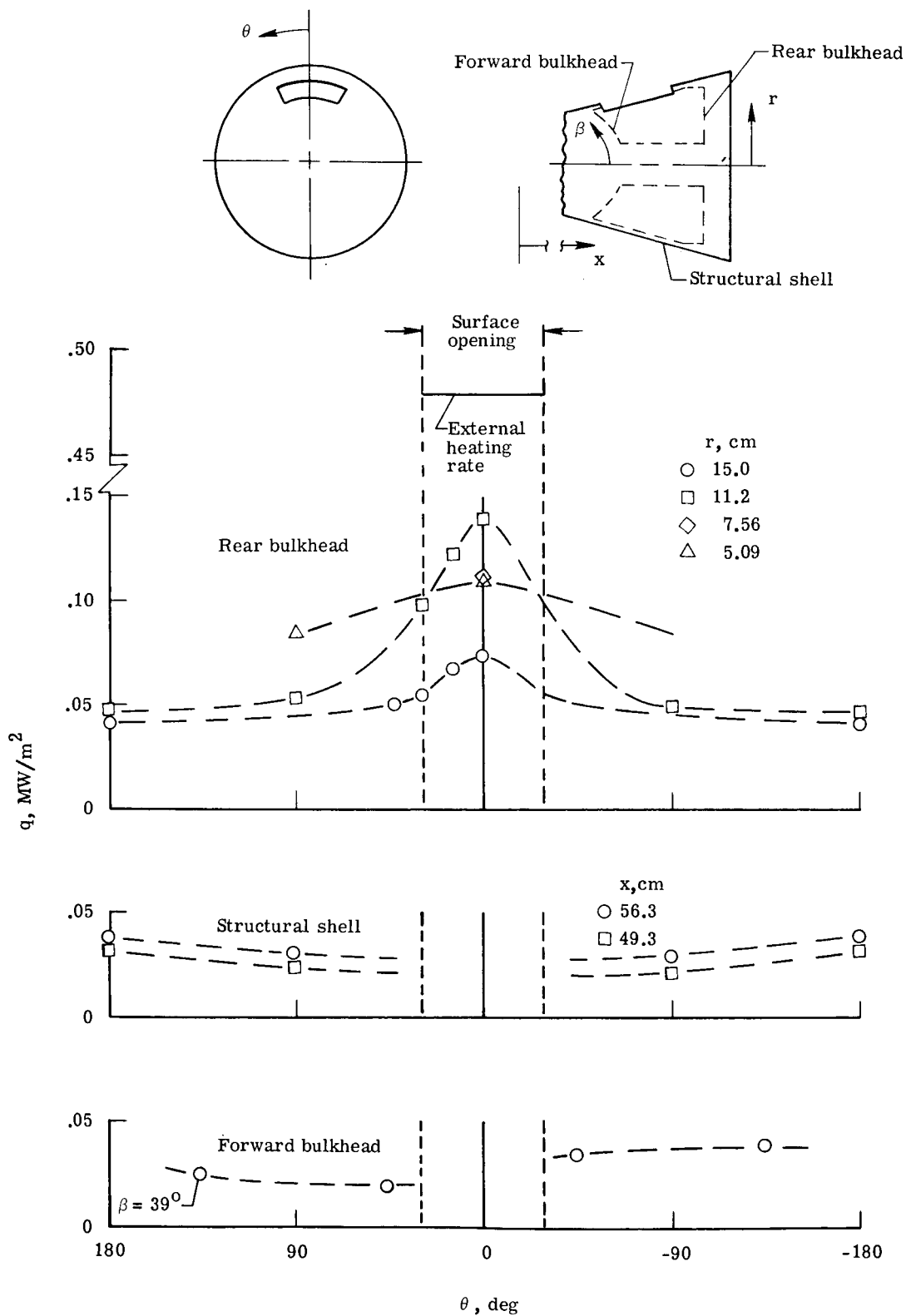
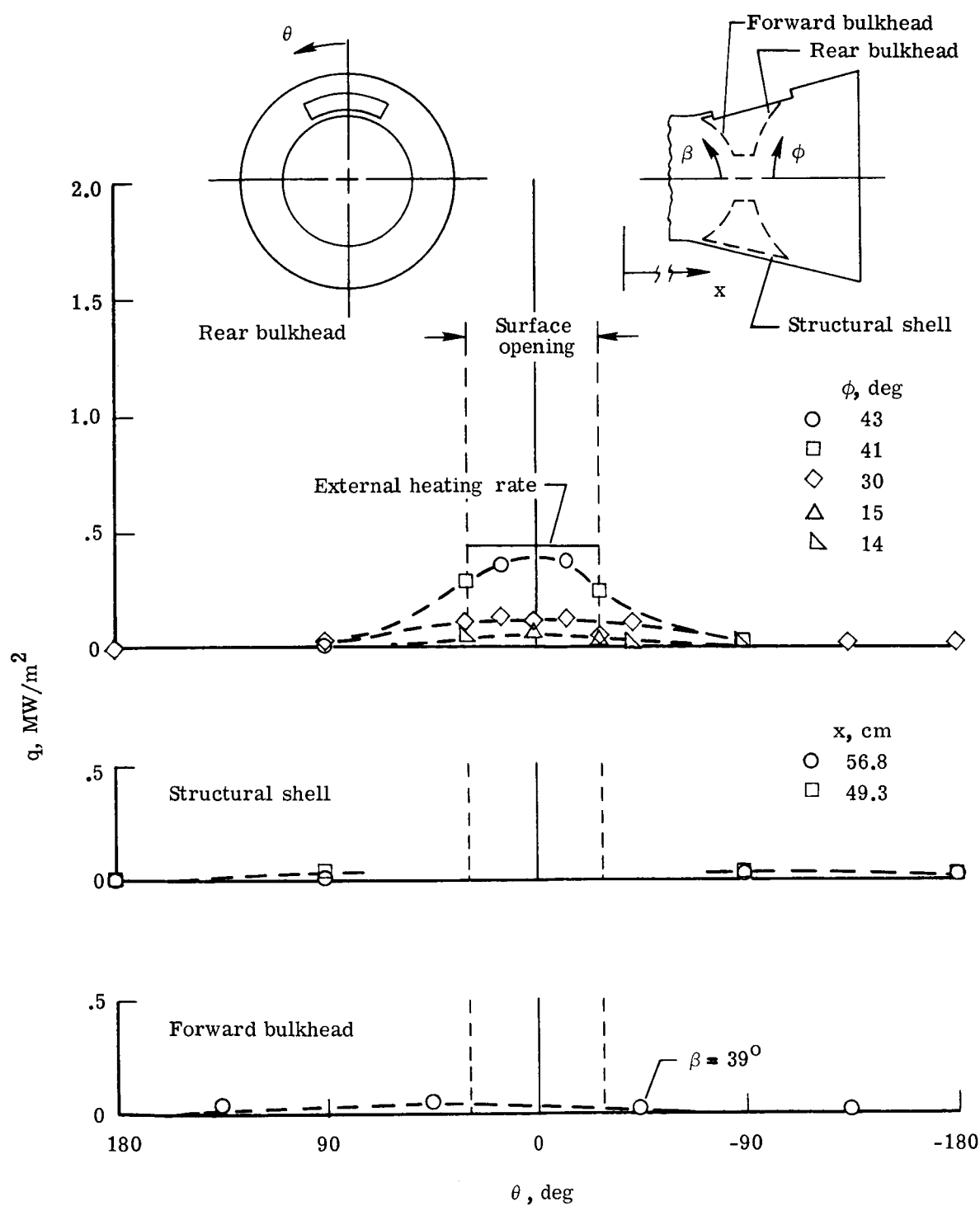
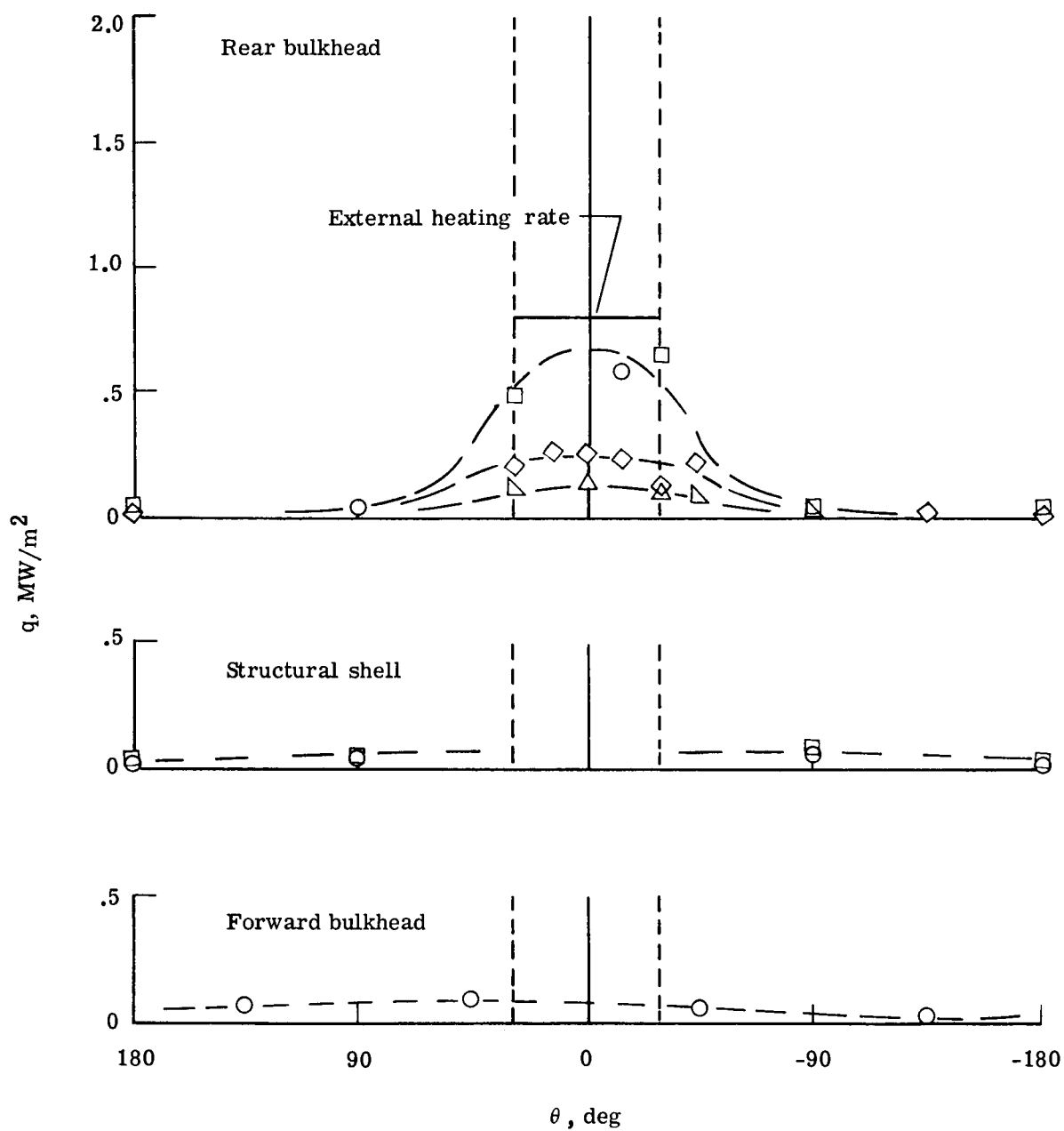


Figure 15.- Angular heating-rate distribution within model A.



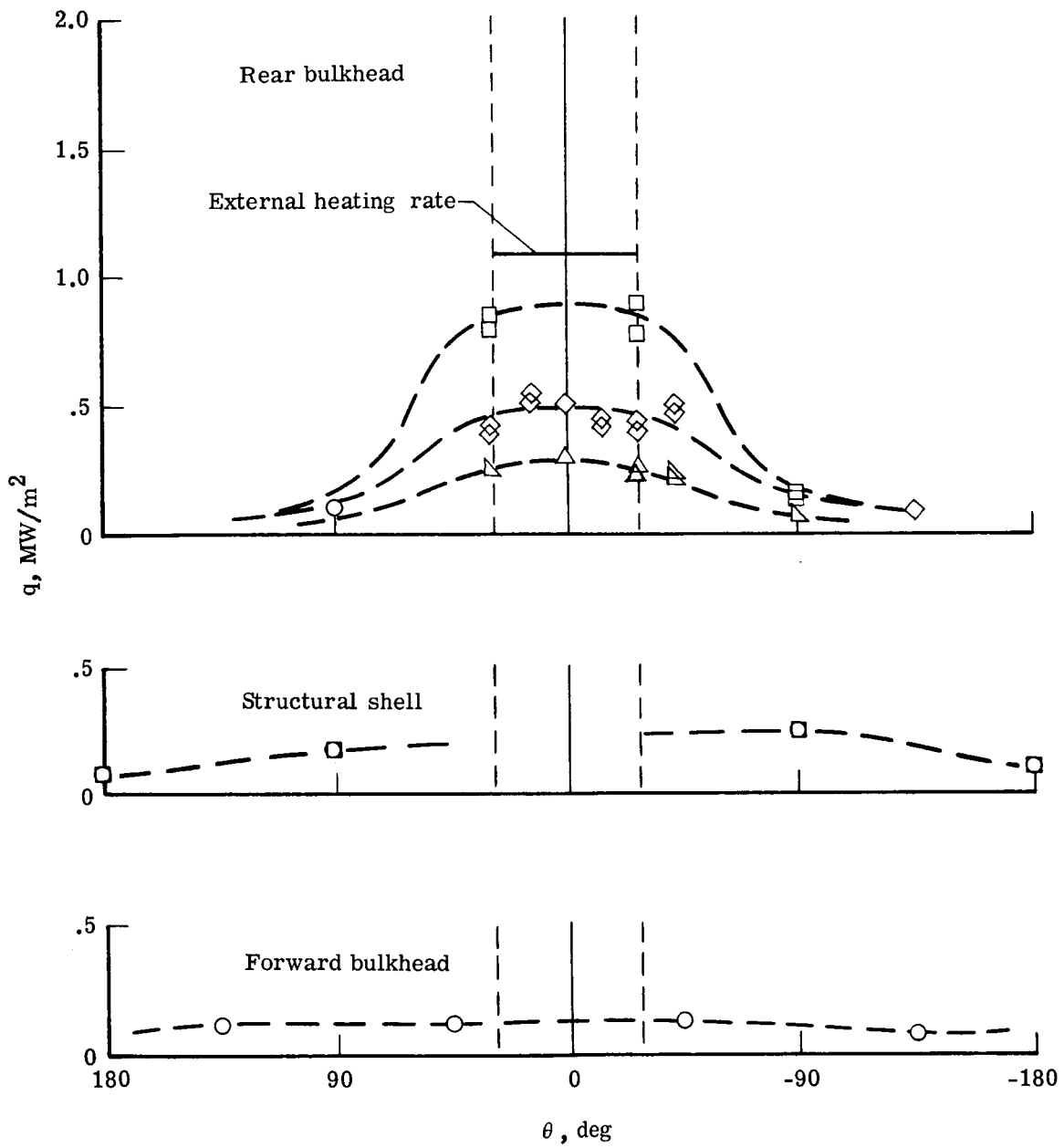
(a) $\alpha = 0^\circ$.

Figure 16.- Angular heating-rate distribution within model B.



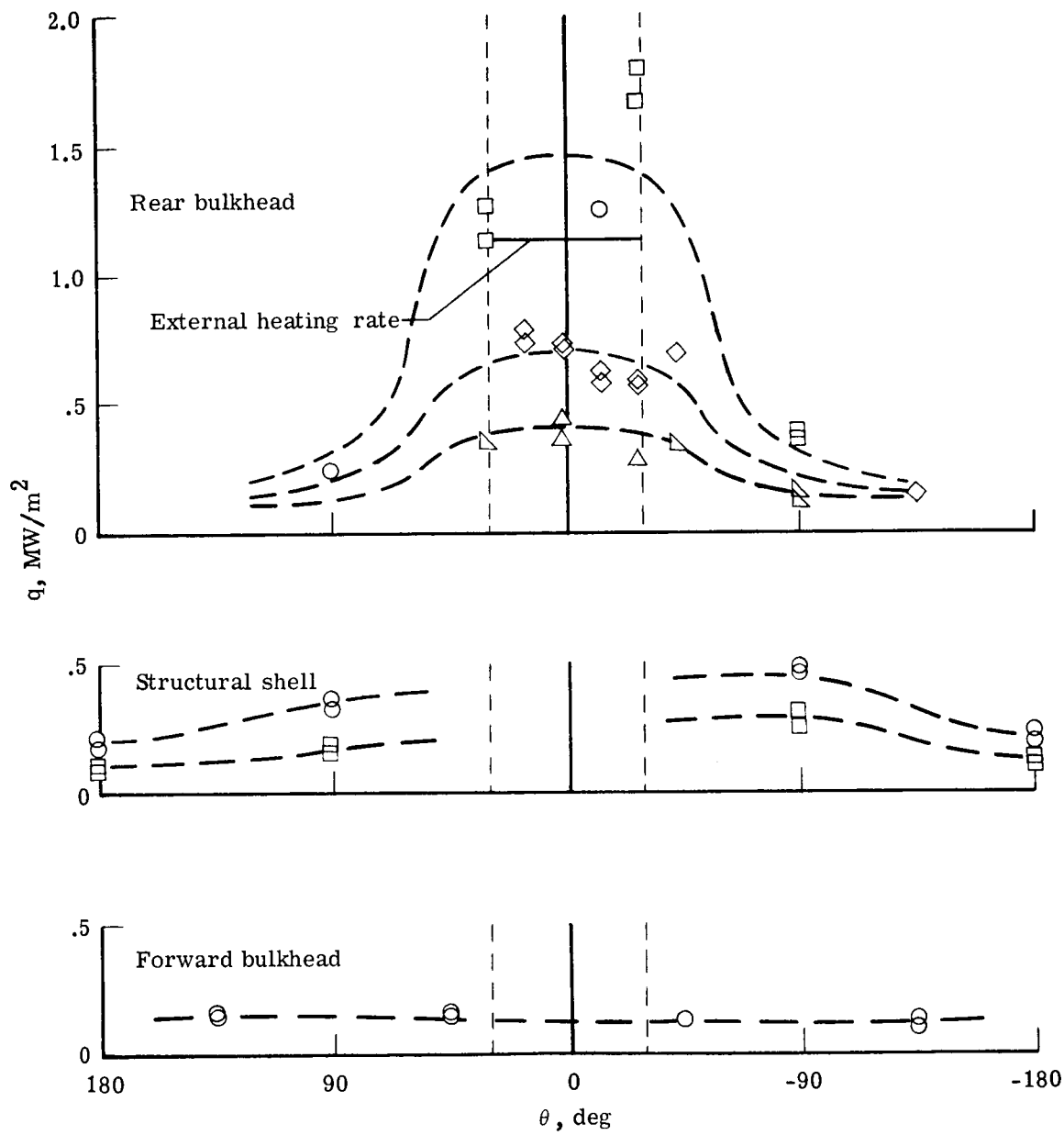
(b) $\alpha = 10^\circ$.

Figure 16.- Continued.



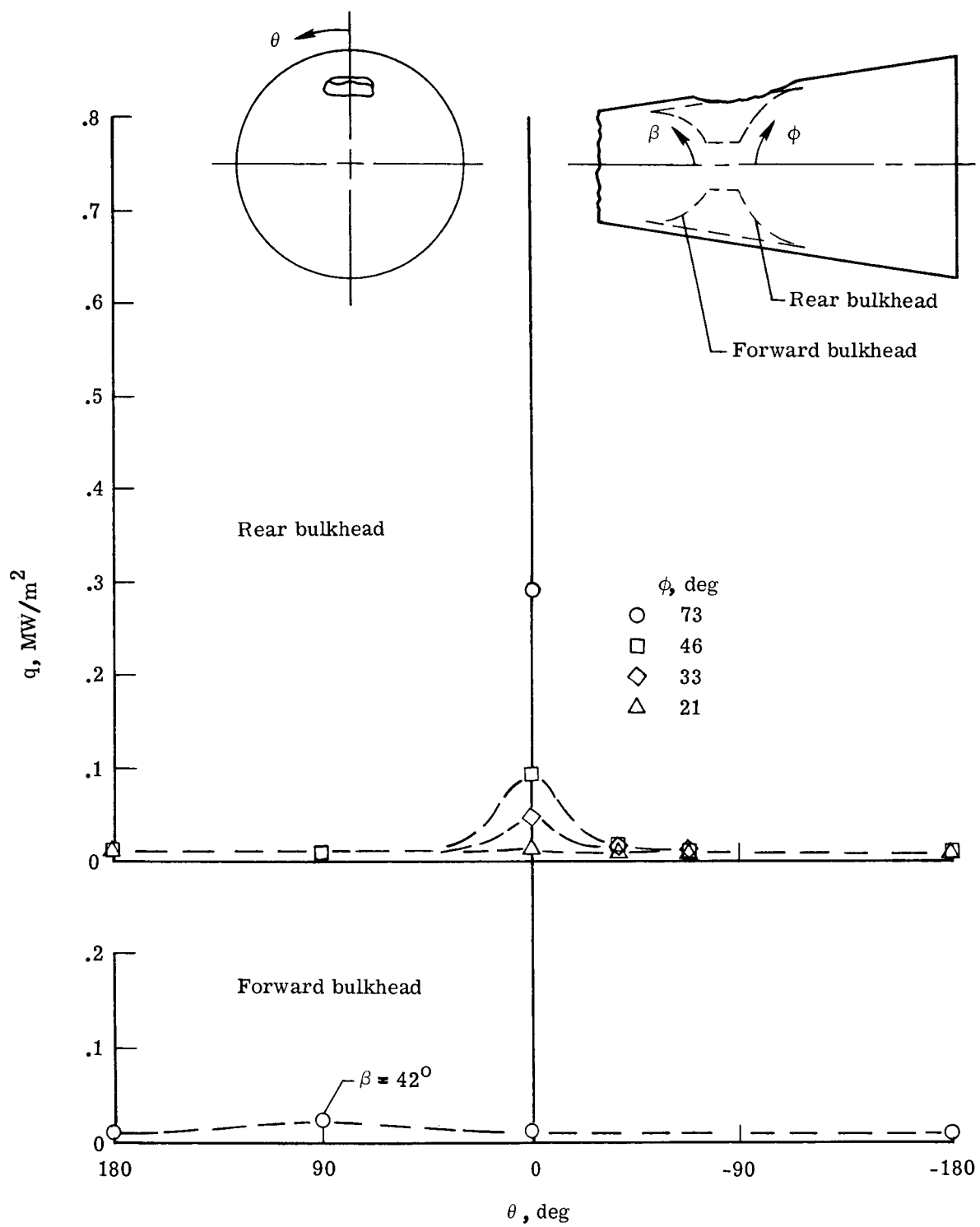
(c) $\alpha = 21^\circ$.

Figure 16.- Continued.



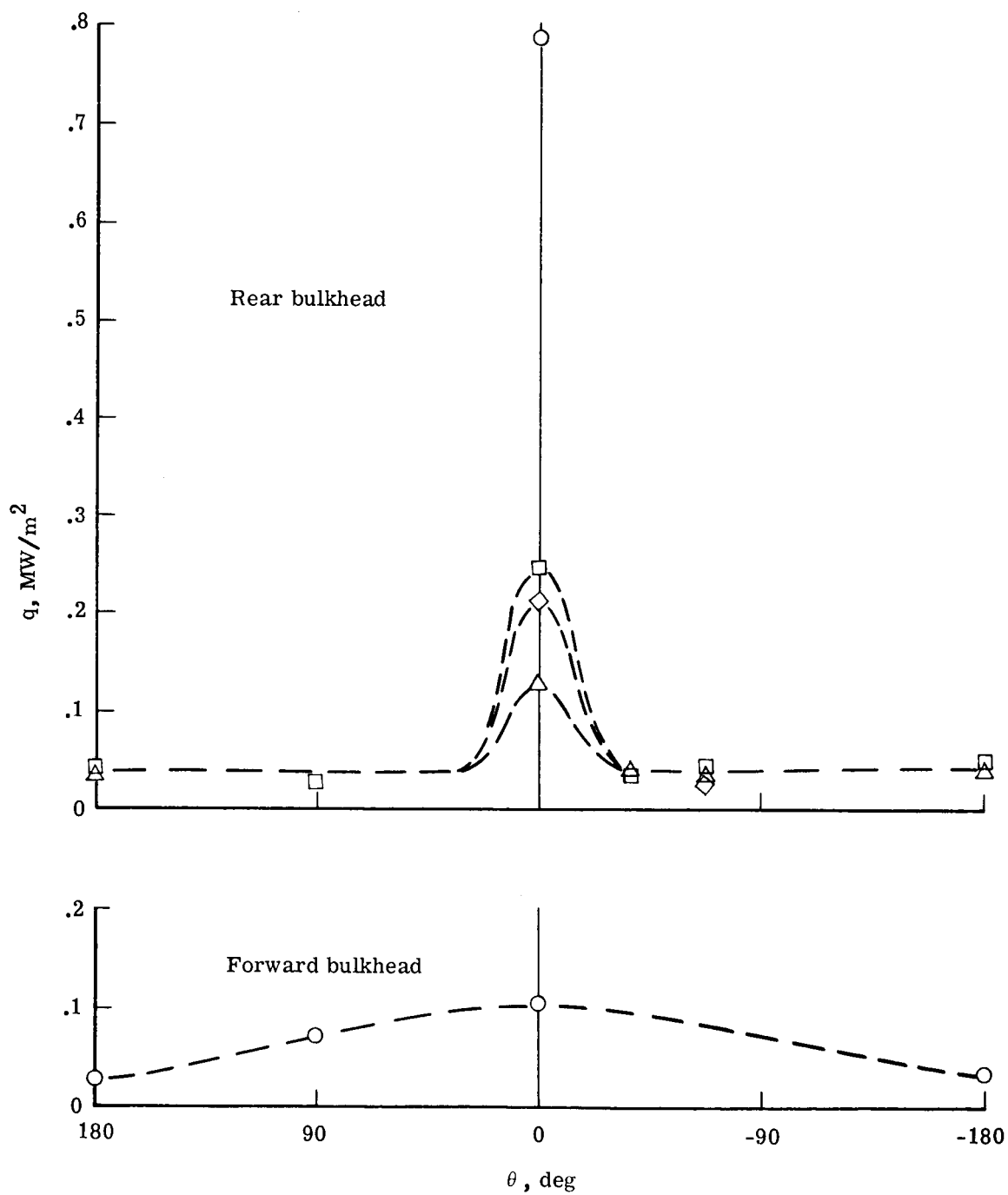
(d) $\alpha = 30^\circ$.

Figure 16.- Concluded.



(a) $\alpha = 0^\circ$.

Figure 17.- Angular heating-rate distribution within model C.



(b) $\alpha = 10^\circ$.

Figure 17.- Concluded.

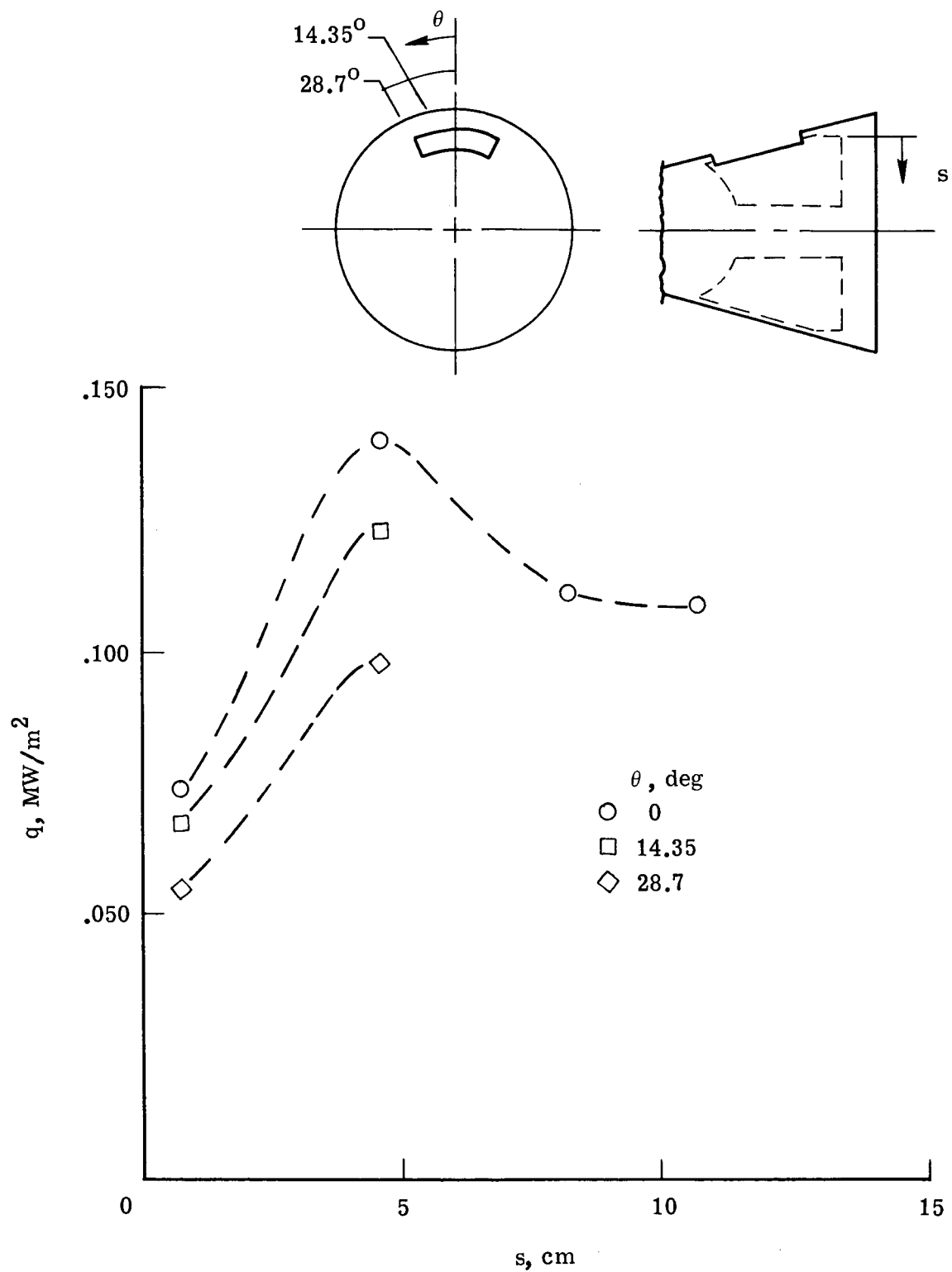


Figure 18.- Heating-rate distribution on the rear bulkhead of model A.

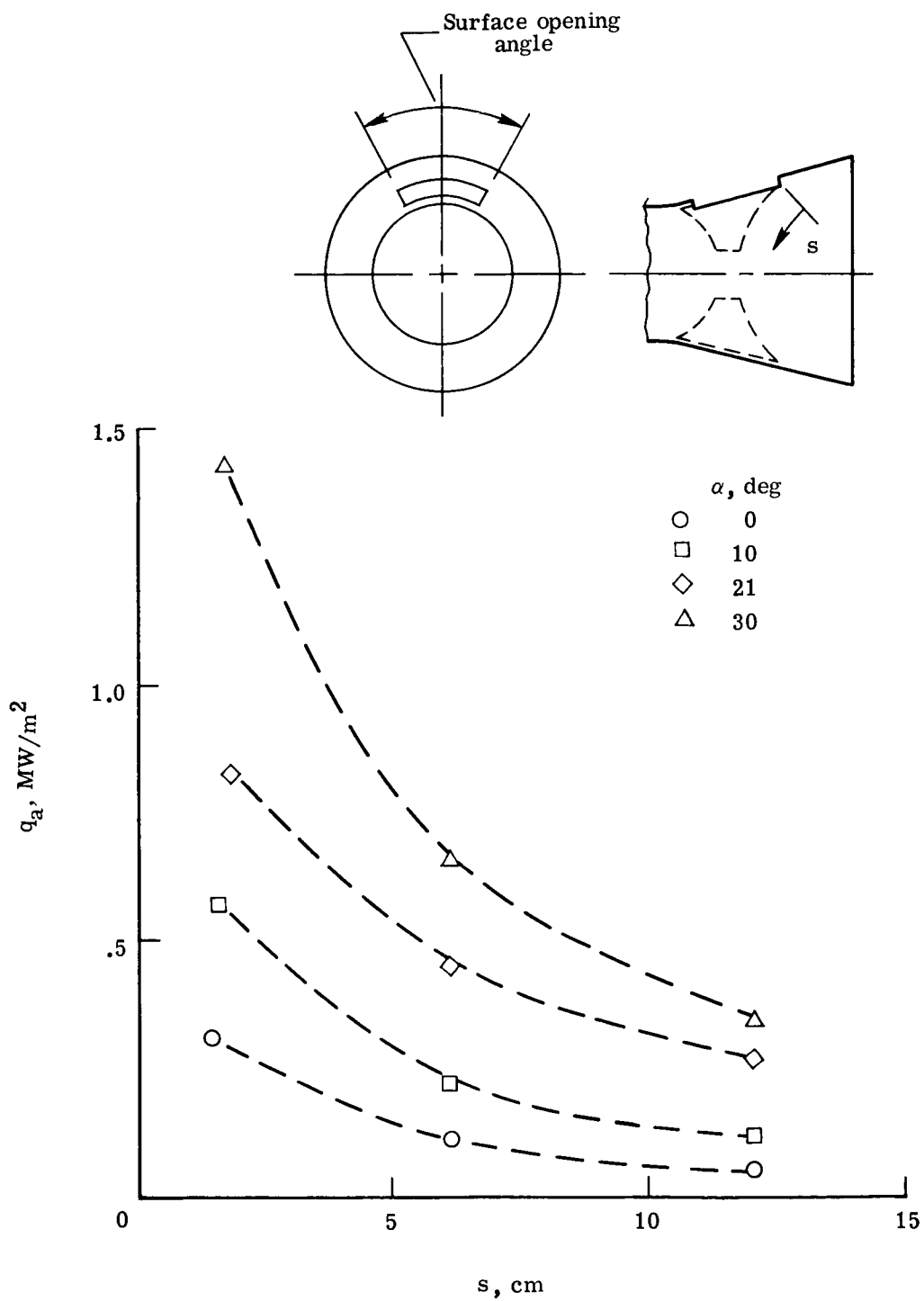


Figure 19.- Heating-rate distribution on the rear bulkhead of model B.

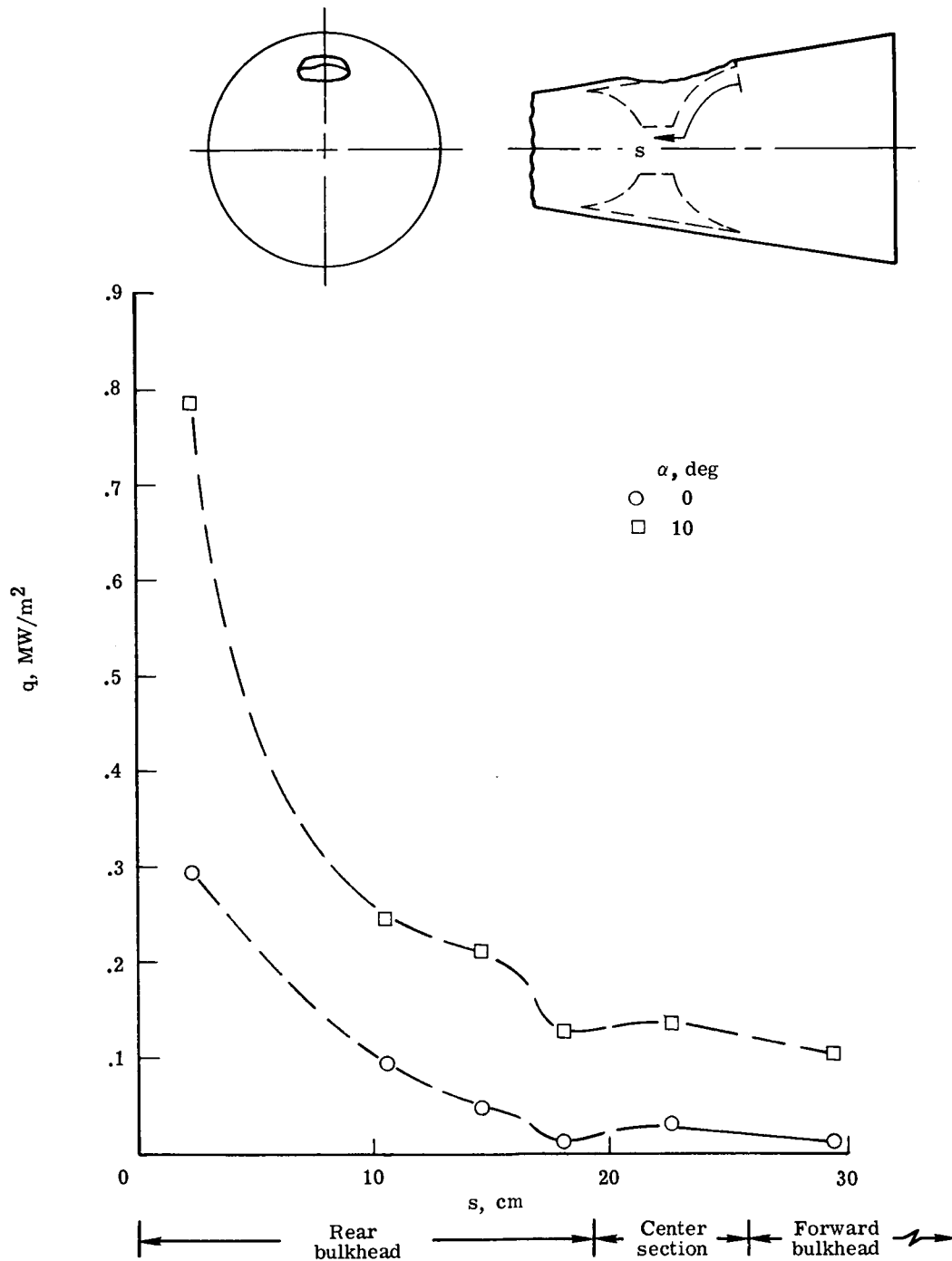


Figure 20.- Heating-rate distribution along the internal flow path in the pitch plane of model C.

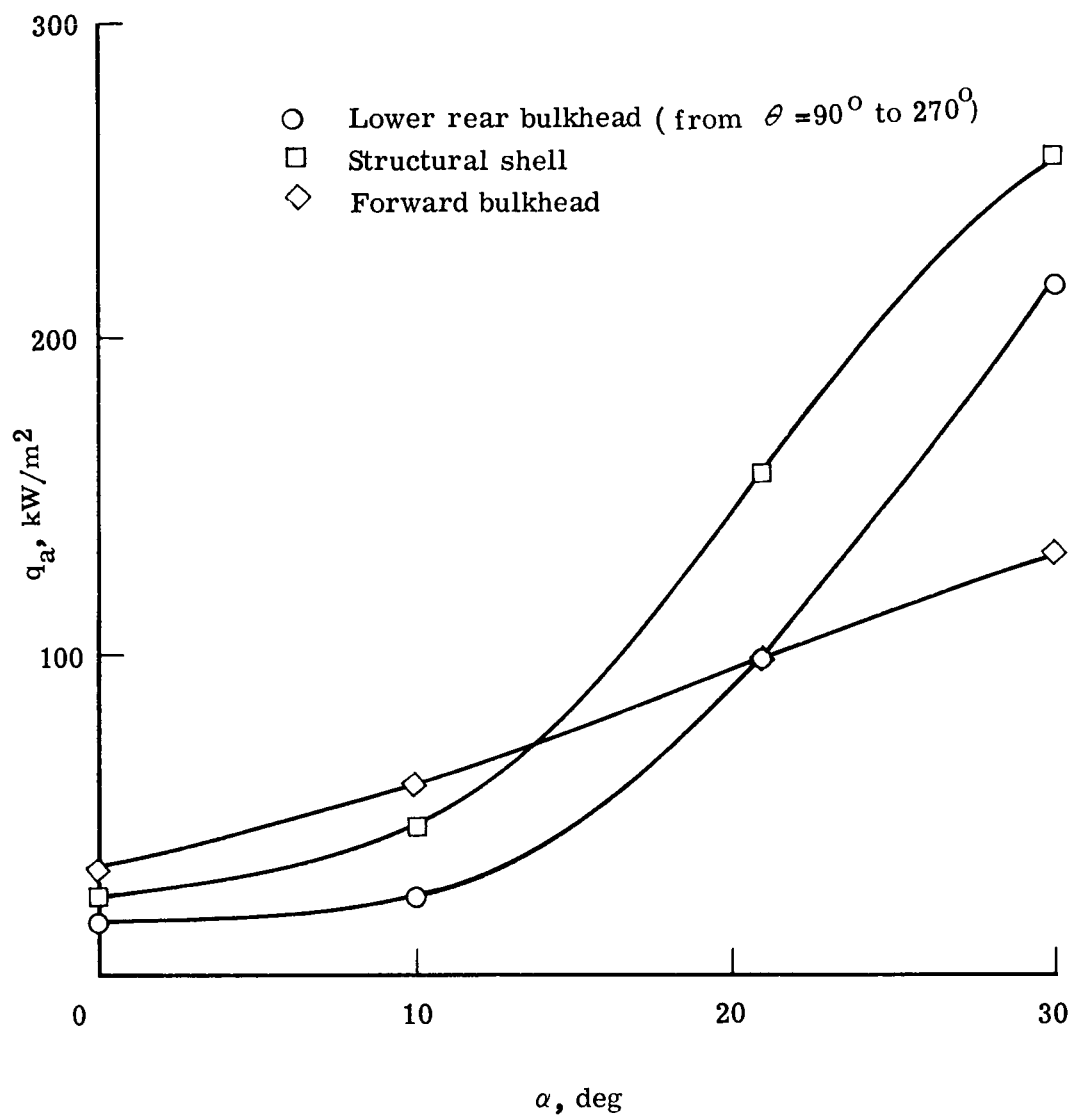


Figure 21.- Variation with α of the average levels of heating to the internal components of model B.